JGR Planets

RESEARCH ARTICLE
10.1029/2023JE007845

Key Points:

- We numerically simulated magmatism in the convecting mantle of the Moon to understand its evolution
- Magma is generated in the deep mantle and ascends to the surface as partially molten plumes driven by melt buoyancy
- Extension of partially molten regions by the plumes causes the observed expansion and active volcanism of the early Moon

Supporting Information:

Supporting Information may be found in the online version of this article.

Correspondence to:

K. U,
u-kenyo0822@g.ecc.u-tokyo.ac.jp

Citation:

U, K., Kameyama, M., & Ogawa, M. (2023). The volcanic and radial expansion/contraction history of the Moon simulated by numerical models of magmatism in the convective mantle. *Journal of Geophysical Research: Planets*, *128*, e2023JE007845. https://doi.org/10.1029/2023JE007845

Received 29 MAR 2023
Accepted 22 AUG 2023

The Volcanic and Radial Expansion/Contraction History of the Moon Simulated by Numerical Models of Magmatism in the Convective Mantle

Ken'yo U[1], Masanori Kameyama[2], and Masaki Ogawa[1]

[1]Department of Earth Sciences and Astronomy, The University of Tokyo, Meguro, Japan, [2]Geodynamics Research Center, Ehime University, Matsuyama, Japan

Abstract To understand the evolution of the Moon, we numerically modeled mantle convection and magmatism in a two-dimensional polar rectangular mantle. Magmatism occurs as an upward permeable flow of magma generated by decompression melting through the convecting matrix. The mantle is assumed to be initially enriched in heat-producing elements (HPEs) and compositionally dense ilmenite-bearing cumulates (IBC) at its base. Here, we newly show that magma generation and migration play a crucial role in the calculated volcanic and radial expansion/contraction history. Magma is generated in the deep mantle by internal heating for the first several hundred million years. A large volume of the generated magma ascends to the surface as partially molten plumes driven by melt buoyancy; the magma generation and ascent cause a volcanic activity and radial expansion of the Moon with the peak at 3.5–4 Gyr ago. Eventually, the Moon begins to radially contract when the mantle solidifies by cooling from the surface boundary. As the mantle is cooled, the activity of partially molten plumes declines but continues for billions of years after the peak because some basal materials enriched in the dense IBC components hold HPEs. The calculated volcanic and radial expansion/contraction history is consistent with the observed history of the Moon. Our simulations suggest that a substantial fraction of the mantle was solid, and there was a basal layer enriched in HPEs and the IBC components at the beginning of the history of the Moon.

Plain Language Summary We developed a numerical model of magmatism in the convecting mantle to understand the volcanic and radial expansion/contraction history of the Moon. In the early period of the calculated history, magma is generated in the deep mantle and ascends to the surface as partially molten plumes driven by melt buoyancy. The plumes cause volcanic activity, and the extension of partially molten regions by magma ascent causes radial expansion of the Moon. In its latter period, however, the Moon contracts with time because partially molten regions solidify as they are cooled from the surface boundary. The activity of partially molten plumes declines but continues for billions of years because some materials that host heat-producing elements (HPEs) are enriched in compositionally dense components and remain in the deep mantle. The calculated history of radius change and volcanism is consistent with the observed lunar history. Our simulations suggest that a substantial fraction of the mantle was solid, and a dense layer enriched in HPEs developed at the base of the mantle at the beginning of the history of the Moon.

1. Introduction

Understanding the mantle evolution of the Moon that is behind its observed history of volcanic activity and radius change has been a long-standing issue in studies of the interiors of terrestrial planets (e.g., Breuer & Moore, 2015; Kirk & Stevenson, 1989; Shearer et al., 2006; Solomon & Chaiken, 1976). The Moon expanded globally by 0.5–5 km in its earlier history until around 3.8 Gyr ago as revealed by the gravity gradiometry data (Andrews-Hanna et al., 2013, 2014; Liang & Andrews-Hanna, 2022; Sawada et al., 2016), and it then globally contracted until today, as suggested from observations of tectonic features on the Moon (Frueh et al., 2023; Yue et al., 2017); some observations of fault scarps (thrust faults) suggest that the contraction for the past 100 Myr is around 1 km or less (e.g., Clark et al., 2017; Klimczak, 2015; Matsuyama et al., 2021; van der Bogert et al., 2018; Watters et al., 2010, 2015). The period when its radius reached the maximum coincides with that when the mare volcanism was active: mare volcanism became more active with time for the first several hundred million years of the lunar history, peaked at 3.5–3.8 Gyr ago, and then declined but continued until around 1.5 Gyr ago (e.g., Hiesinger et al., 2000, 2003; Morota et al., 2011; Whitten & Head, 2015). To clarify the mantle evolution that has

caused the observed features of the lunar history, we developed a two-dimensional (2-D) polar rectangular model of the lunar mantle evolution where mantle convection and magmatism that transport heat, mass, and incompatible heat-producing elements (HPEs) are considered.

Various numerical models of mantle evolution have been advanced to account for the observed radius change, in particular, the early expansion of the Moon (e.g., Shearer et al., 2006; Solomon, 1986). Classical spherically symmetric one-dimensional (1-D) models, where the radius change occurs only thermally, show that the early expansion is reproduced in the models when the temperature in the deep mantle is initially 1100 K or less; these models suggest that subsequent temperature rise of more than 700 K should be caused by internal heating in the deep mantle to account for the observed early expansion (Solomon & Chaiken, 1976). In the model of Kirk and Stevenson (1989) that also takes volume change from compositional differentiation of the mantle into account, the early expansion occurs even when the initial temperature of the deep mantle is as high as 1200 K. Giant impact hypotheses for the origin of the Moon, however, suggest a much higher initial temperature for the Moon (e.g., Canup, 2004; Cuk & Stewart, 2012; Lock et al., 2018; Pritchard & Stevenson, 2000; Rufu et al., 2017; Stevenson, 1987). The mantle is expected to have been mostly molten to form the magma ocean after the impact (e.g., Hosono et al., 2019; Newsom & Taylor, 1989). Even at the end of the mantle overturn, which is expected to have occurred after solidification of the magma ocean, the temperature of the deep mantle is still suggested to have been as high as about 1800–1900 K (e.g., Alley & Parmentier, 1998; Boukaré et al., 2018; Hess & Parmentier, 1995, 2001; H. Li et al., 2019). When such a high initial temperature is assumed, the early expansion of the Moon is difficult to reproduce in the classical thermal history models (e.g., Solomon, 1986; Solomon & Chaiken, 1976). The early expansion consistent with the observed history does not occur in three-dimensional (3-D) spherical models where mantle convection is also considered. In the models of N. Zhang et al. (2013a, 2013b), the early expansion does occur owing to internal heating, but the amplitude of the expansion is much smaller than the observed value (e.g., Andrews-Hanna et al., 2013), and the period when the expansion occurs is longer than 1 Gyr. In some models where the uppermost mantle is locally more enriched in HPEs on the nearside as observed for the Procellarum KREEP terrane, or PKT (Laneuville et al., 2013; Wieczorek & Phillips, 2000), the expansion occurs only on the nearside and is too large to account for the observed expansion (e.g., Liang & Andrews-Hanna, 2022). To understand the observed early expansion of the Moon, U et al. (2022) constructed a 1-D spherically symmetric model where volume change of the mantle by melting is considered in addition to thermal expansion. The mantle expands by a few kilometers for the first several hundred million years of the calculated history when partially molten regions extend in the mantle by internal heating, suggesting that melting of the mantle played an important role in the early expansion of the Moon. Yet, mantle convection is not considered in this model.

Various numerical models have been advanced to account for the long-lasting volcanism of the Moon, too (e.g., Breuer & Moore, 2015; Shearer & Papike, 1999). Some earlier models show that partially molten regions persist for billions of years in the upper mantle when the surface is covered with a crust enriched in HPEs or a blanketing regolith layer (Konrad & Spohn, 1997; Spohn et al., 2001; Ziethe et al., 2009). In models where the uppermost mantle in the nearside is more enriched in HPEs than that in the farside, the mantle has been partially molten for more than 3 billion years (Laneuville et al., 2013, 2014, 2018). In these models, however, the distribution of HPEs is spatially fixed or transported only by mantle convection; extraction of HPEs from the mantle to the crust by magmatism, which is known to reduce the activity of magmatism (e.g., Cassen & Reynolds, 1973; Cassen et al., 1979; Ogawa, 2014), is not considered. In a model of Ogawa (2018a) where extraction of HPEs from the mantle by migrating magma is considered, partially molten regions have been completely cooled, and magmatism stops within the first 2 Gyr of the calculated history; the end of this magmatism is too early to account for the lunar mare volcanism (e.g., Hiesinger et al., 2003). It is also important to consider not only HPE-extraction by migrating magma, but also the effects of structural evolution of the mantle in studies of the lunar volcanism (e.g., Hess & Parmentier, 1995; Stegman et al., 2003; N. Zhang et al., 2013a; W. B. Zhang et al., 2022; Zhong et al., 2000). In the early period of the Moon, a compositionally dense layer, which is enriched in HPEs and ilmenite-bearing cumulates (IBC) components, is suggested to have developed at the base of the mantle by crystal fractionation in the magma ocean and subsequent mantle overturn (e.g., Elkins-Tanton et al., 2011; Hess & Parmentier, 1995; Snyder et al., 1992). Earlier mantle convection models suggest that the basal layer becomes thermally buoyant owing to internal heating and eventually migrates upward to the surface as hot plumes to cause mare volcanism after around 4 Gyr ago (e.g., Hess & Parmentier, 1995; Zhong et al., 2000). Whether or not the basal layer rises, however, depends on the compositional density contrast between the layer and the overlying

mantle. These models assume conditions where the density contrast is low enough to allow the basal layer to rise by thermal convection (see Figure 1 in Le Bars and Davaille (2004)). The density contrast after mantle overturn is unclear and is influenced by the initial condition of overturn models (e.g., H. Li et al., 2019; Yu et al., 2019; W. B. Zhang et al., 2022); further studies with various density content are necessary to fully understand to effects of compositional mantle structure on volcanic history.

To understand the mantle evolution in the Moon that is constrained by its volcanic and radial expansion/contraction history, we extend the 1-D spherically symmetric model we developed earlier (U et al., 2022) to a 2-D polar rectangular model. In our previous model, we considered magma generation by internal heating and magma migration that transports heat, HPE, and mass as well as volume change of the mantle by melting. In addition to these effects, here in this study, we also include the effects of mantle convection. Heat and mass transport by mantle convection plays an important role in mantle evolution (e.g., Spohn et al., 2001; N. Zhang et al., 2017). Upwelling flows of mantle convection generate magma by decompression melting, which also affects the mantle evolution of the Moon (e.g., Ogawa, 2020). We also take the effects of compositional layering at the base of the mantle formed by the magma ocean and mantle overturn on the subsequent mantle evolution into account. This model is an extension of the one presented in Ogawa (2014, 2018a) in that we considered the volume change of mantle by melting, more systematically studied the effects of the initial condition, and calculated in a 2-D polar rectangle rather than a rectangle.

2. Model Description

A finite difference numerical code calculates the energy, mass, and momentum equations for mantle magmatism and mantle convection in a two-dimensional polar rectangle $R = [(r, \theta)|\ 385\ \text{km} \le r \le 1735\ \text{km},\ 0 \le \theta \le \pi]$ on a mesh with 128 (radial direction) times 256 (lateral direction) mesh points under the Boussinesq approximation, where the inner and the outer radii correspond to the core and planetary radii, respectively, of the Moon (e.g., Viswanathan et al., 2019; Weber et al., 2011; Yan et al., 2015). The mantle contains incompatible HPEs that decay with time. The mantle is considered a Newtonian fluid with a strongly T-dependent viscosity, and convection is driven by thermal, composition, and melt buoyancy. The convecting materials are a binary eutectic system between olivine-rich materials and IBC. Magmatism occurs as generation of basaltic magma enriched in IBC materials and HPEs by decompression melting and internal heating together with upward permeable flow of the generated magma through the matrix (McKenzie, 1984; Vander Kaaden et al., 2015); the permeable flow is driven by the buoyancy of the melt. We assumed that the solid phase is always denser than the melt phase. Some earlier studies, however, suggest that IBC-rich magma can be denser than the coexisting matrix in the deep mantle of the Moon (e.g., Sakamaki et al., 2010; van Kan Parker et al., 2012; Xu et al., 2022). We also examined how this melt-solid density inversion can influence our numerical results (Section 3.4). As mentioned there, we found that the density inversion does not affect the overall features of mantle evolution.

The crust of 35 km in thickness is placed on the top of the mantle (Wieczorek et al., 2013). The thermal diffusivity of the crust is about half that of the mantle, and hence the crust serves as a blanketing layer (Ziethe et al., 2009). The temperature is fixed at $T_{\text{sur}} = 270$ K on the surface boundary, while the core is modeled as a heat bath of uniform temperature; the vertical sidewalls are insulating. All of the boundaries are impermeable for both magma and matrix and are shear stress-free. In the initial condition, we assume that the deep mantle is more enriched in HPEs and the IBC components than the shallower mantle as earlier models of mantle differentiation by the magma ocean and subsequent mantle overturn suggest (e.g., Hess & Parmentier, 1995; Moriarty III et al., 2021; Ringwood & Kesson, 1976). Several previous studies, however, suggest that a portion of the IBC materials enriched in HPEs persist just beneath the crust even after mantle overturn (e.g., Schwinger & Breuer, 2022; Yu et al., 2019; Zhao et al., 2019). Instead of explicitly simulating these remains of HPE-enriched materials, we assume that the crust is uniformly enriched in HPEs.

2.1. The Properties of Materials

The convecting material is a binary eutectic system. The composition is written as $A_{\xi}B_{1-\xi}$; the mantle materials are modeled as a mixture of olivine-rich materials (A) with a density of 3,300 kg m^{-3} (Elkins-Tanton et al., 2011) and the IBC (B) with a density of 3,745 kg m^{-3} (Elkins-Tanton et al., 2011; Rapp & Draper, 2018; Shearer et al., 2006; Snyder et al., 1992). The eutectic composition is $A_{0.1}B_{0.9}$ ($\xi_e = 0.1$) which corresponds to the basaltic

Table 1
The Meanings of the Symbols and Their Values

Symbol	Meaning	Value
T_{sur}	Surface temperature	270 K
T_0	Solidus at the surface	1360 K
r_p	Radius of the surface	1,735 km
r_c	Radius of the core-mantle boundary (CMB)	385 km
r_{crst}	Radius of the Moho	1,700 km
ρ_0	Reference density	3,300 kg m^{-3}
κ	Thermal diffusivity of the mantle	6×10^{-7} m^2 s^{-1}
κ_{edd}	Eddy diffusivity in largely molten region	100κ at $\phi > 0.4$
g_{sur}	Gravitational acceleration at the surface	1.62 m s^{-2}
g_c	Gravitational acceleration at the CMB	0.55 m s^{-2}
Δh	Latent heat of melting	657 kJ kg^{-1}
C_p	Specific heat	1240 J K^{-1} kg^{-1}
η_0	Reference viscosity	$10^{20} - 10^{22}$ Pa s
η_{melt}	Melt viscosity	1 − 20 Pa s
E_T	Sensitivity of viscosity to temperature	11.3×10^{-3} K^{-1}
ϕ_0	Reference melt-content	0.05
k_{ϕ_0}	Reference permeability	8.6×10^{-15} m^2
α_m	Thermal expansivity in the mantle	3×10^{-5} K^{-1}
α_c	Thermal expansivity in the core	9×10^{-5} K^{-1}

composition enriched in the IBC components (see Appendix A for the detail of the thermodynamic formulation).

The density ρ is written as

$$\rho = (1-\phi)\rho_s + \phi\rho_l. \quad (1)$$

where ρ_s is the density of solid phase, ρ_l the density of melt phase, and ϕ the melt-content. The densities depend on the temperature T and the content of the end-member A in the solid phase ξ_s and that in the melt phase ξ_l as

$$\rho_s = \rho_0[1 - \alpha(T - T_{sur}) + \beta(1 - \xi_s)], \quad (2)$$

and

$$\rho_l = \rho_0\left\{1 - \alpha(T - T_{sur}) + \beta(1 - \xi_l) - \frac{\Delta v_l}{v_0}[1 + \beta(1 - \xi_l)]\right\}, \quad (3)$$

where ρ_0 is the reference density; α the thermal expansivity; $\beta = 0.135$ a constant estimated from the density of olivine-rich end-member A and that of the IBC end-member B. The temperature is calculated from the energy equation (Equation A3 in Appendix A) that describes the evolution of the "reduced" enthalpy h:

$$h = C_p T + \phi\Delta h(1 + G), \quad (4)$$

where C_p is the specific heat; Δh the latent heat of melting; G the function which depends on $\Delta v_l/v_0$ (see Equation 10 below). $\Delta v_l/v_0$ expresses the amount of density reduction by melting as

$$\frac{\Delta v_l}{v_0} = \frac{1}{\rho_0}\left[\Delta\rho_\infty + \frac{\Delta\rho_{zero} - \Delta\rho_\infty}{(P/\lambda + 1)^2}\right]. \quad (5)$$

Here, $\Delta\rho_\infty/\rho_0 = 0.005$ is the dimensionless density difference between solid and liquid phases when pressure is infinity, and $\Delta\rho_{zero}/\rho_0 = 0.22$ that at zero-pressure. $P = -\int_{r_p}^{r} \rho_0 g dr$ is the pressure; the gravitational acceleration g depends on the depth as $g = g_{sur} - (g_{sur} - g_c)\frac{r_p - r}{r_p - r_c}$ (Garcia et al., 2011, 2012). We assumed the value of $\lambda = 16.42$ GPa so that the solidus temperature is calculated from the Clausius-Clapeyron relationship (see Equations 9 and 10 below) becomes close to that in the lunar mantle (Garcia et al., 2011, 2012; Katz et al., 2003).

Magma is generated by decompression melting and internal heating. The generated magma migrates upward as a permeable flow through the coexisting matrix driven by its buoyancy. Migrating magma transports heat, basaltic materials, and HPEs. The difference between the velocity of magma $\mathbf{u}$ and that of matrix $\mathbf{U}$ is proportional to the density difference between them as

$$\mathbf{u} - \mathbf{U} = \frac{k_\phi}{\phi\eta_{melt}} g(\rho_s - \rho_l)\mathbf{e_r}, \quad (6)$$

where k_ϕ is the permeability that depends on the melt-content ϕ as

$$k_\phi = k_{\phi_0}\left(\frac{\phi}{\phi_0}\right)^3 \quad (7)$$

(McKenzie, 1984) and $\mathbf{e_r}$ is the unit vector in the radial direction. We assumed that $\phi_0 = 0.05$ and truncated ϕ at 0.4 for numerical reasons. The assumed range of k_{ϕ_0} given in Table 1 is based on the earlier works of McKenzie (1984) and Miller et al. (2014). In the top-most 150 km of the polar rectangular, we inserted $\phi' = \max(\phi, \phi_e)$ into the ϕ in Equation 7 to mimic magma migration that occurs by crack propagation in the crust and the uppermost mantle of the Moon (Head & Wilson, 2017; Wilson & Head, 2017)

$$k_\phi = k_{\phi_0}\frac{[\max(\phi, \phi_e)]^3}{\phi_0^3}, \quad (8)$$

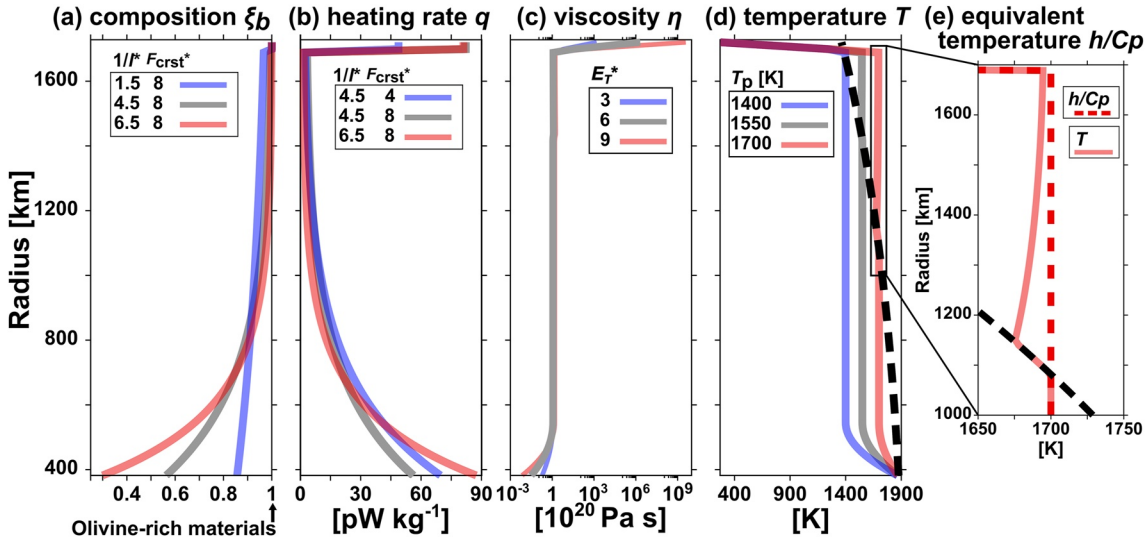

Figure 1. An illustration of the initial distributions of (a) bulk composition ξ_b, (b) internal heating rate q, (c) viscosity η at $\eta_0 = 10^{20}$ Pa s and $T_p = 1550$ K, (d) temperature T, and (e) equivalent temperature h/C_p in the depth range shown by the rectangle in (d). In (d) and (e), the black dashed line is the solidus which is calculated by Equation 9. Note that $h/C_p = T$ holds for regions below the solidus (Equation 4). The meaning of variable parameters l^*, F^*_{crst}, E^*_T, and T_p is described in Table 2.

where $\phi_e = 0.035$ is an "effective porosity" for magma-migration by crack propagation (Kameyama et al., 1996).

The solidus temperature $T_{solidus}$ depends on the pressure as

$$T_{solidus} = T_0(1 + G), \tag{9}$$

where

$$G = \frac{1}{\rho_0 \Delta h} \int_0^P \frac{\Delta v_l}{v_0}\, dP. \tag{10}$$

Here, T_0 is the solidus temperature at the surface (Katz et al., 2003).

The viscosity of the mantle η depends on temperature as

$$\eta = \eta_0 \exp[E_T(T_{ref} - T)], \tag{11}$$

where η_0 is the reference viscosity; $T_{ref} = 1575$ K is the reference temperature. E_T is the sensitivity of viscosity to temperature; the adopted default value of E_T is 11.3×10^{-3} K^{-1} ($E^*_T = 6$, see Section 2.3 below) which implies that the viscosity decreases by a factor of 3 as temperature increases by 100 K (Figure 1c). This range of viscosity variation is appropriate for Newtonian rheology to mimic thermal convection in mantle materials (Dumoulin et al., 1999). In this study, we assumed that the viscosity of the mantle depends only on the temperature for simplicity. Some earlier studies, however, suggest that the viscosity depends on the contents of melt

Table 2
The Variable Parameters of the Numerical Models

Variable parameter	Meaning	Range of value
M^*	Dimensionless reference permeability	5–100
Ra	Rayleigh number	2.15×10^4–10^6
E^*_T	Dimensionless sensitivity of viscosity to temperature	3–9
T_p	The initial potential temperature at depths	1400–1700 K
l^*	The thickness of the overturned layer after mantle overturn	1/6.5–1/1.5
F^*_{crst}	Concentration ratio of HPEs in the crust to the mantle	4–32

and IBC components (e.g., Dygert et al., 2016; Hirth & Kohlstedt, 2003; H. Li et al., 2019; Mei et al., 2002; Scott & Kohlstedt, 2006; N. Zhang et al., 2017). We examined how the reduction of viscosity by melting and IBC components can affect our numerical results in Section 3.3. As mentioned there, we confirmed that both the ϕ-dependence and IBC-dependence of viscosity do not significantly affect the overall features of mantle evolution although found that the ϕ-dependence suppresses "melt-fingers," both of which we will describe in Section 3 below.

In the estimate of the lunar radial expansion, we consider the effect of melting as well as thermal expansion/contraction; the radius change ΔR is given by

$$\Delta R = \frac{1}{r_p}\left[\frac{\alpha_c \Delta T_c}{2} r_c^2 + \int_{r_c}^{r_p}\int_0^{\pi}\left(\alpha_m \Delta T + \frac{\Delta v_l}{v_0}\Delta\phi\right) r dr d\theta\right]. \quad (12)$$

In this equation, the first and second terms in the bracket of the right-hand side represent the volume changes of the core and the mantle, respectively. Here, α_c is the thermal expansivity of the core, $\Delta T_c \equiv T_c(t) - T_c(t=0)$ is the deviation of the temperature T_c in the core at the elapsed time t from its initial value $T_c(t=0)$, and $\Delta T \equiv T(r, \theta, t) - T(r, \theta, t=0)$ and $\Delta\phi \equiv \phi(r, \theta, t) - \phi(r, \theta, t=0)$ are the deviations in the temperature T and melt-content ϕ in the mantle from their initial values, respectively. We assume that the initial condition in this model is the state immediately after mantle overturn (see below), based on the fact that the tectonic features of expansion/contraction in the crust are not recorded during the solidification of the magma ocean (Elkins-Tanton & Bercovici, 2014).

2.2. The Initial Condition

The initial thermo-chemical state of the mantle is specified by the initial distributions of heating rate q, bulk composition ξ_b, and "reduced" enthalpy h. Here, the bulk composition is calculated from the composition of the solid phase ξ_s and that of the liquid phase ξ_l

$$\xi_b = (1-\phi)\xi_s + \phi\xi_l. \quad (13)$$

Figure 1 shows an example of the initial distributions of these quantities (see Appendix B for the equations that describe the distributions). This initial condition is motivated by earlier models of the mantle overturn that is expected to have occurred after the solidification of the magma ocean (e.g., Alley & Parmentier, 1998; Boukaré et al., 2018; Rapp & Draper, 2018; Snyder et al., 1992). In the last stage of crystal fractionation of the magma ocean, a dense layer of the IBC enriched in HPEs develops at the top of the mantle. This layer is expected to sink down to the base of the mantle due to gravitational instability called mantle overturn (e.g., de Vries et al., 2010; Hess & Parmentier, 1995; Ringwood & Kesson, 1976). To simulate the layering at the base of the mantle formed by the overturn, we assumed that the internal heating rate q and the content of the IBC components exponentially increase with depth as $\exp\left[-(r-r_c)/l\right]$ where l represents the thickness of the overturned layer (Figures 1a and 1b). In Figure 1b, we adjusted the initial value of q so that its average in the entire calculated polar rectangle becomes equal to the average value for the bulk silicate Moon. The internal heating rate in the topmost 35 km is also higher than the average value for the mantle by a factor of F^*_{crst}. We assumed this enriched layer to mimic the crust and the KREEP (K, rare earth elements, and P-rich material) layer of the Moon (e.g., Ringwood & Kesson, 1976), which persist even after the mantle overturn (e.g., Zhao et al., 2019). As for the thermal initial condition, we assumed $h/C_p = T_p$ in the entire mantle except around the top and bottom boundaries (Figures 1d and 1e). Note that T_p is the actual temperature in the mid-mantle where materials are solid (Equation 4). For more details of the initial q, ξ_b, and h-distributions, see Appendix B.

2.3. The Parameter Values

We carried out numerical experiments at various values of the non-dimensional reference permeability $M^* \equiv \frac{k_{\phi_0}\rho_0 g_{sur} L}{\kappa\eta_{melt}}$ (see Equation A15) and Rayleigh number $Ra \equiv \frac{\rho_0\alpha_m(\Delta h/C_p)g_{sur}L^3}{\kappa\eta_0}$ (see Equation A13), as well as the sensitivity of viscosity to temperature $E^*_T = E_T\Delta h/C_p$, the potential temperature T_p, the thickness of the overturned layer $l^* = l/L$, and the ratio of the concentration of HPEs in the crust to that in the mantle F^*_{crst}, where $L = r_p - r_c$, is the depth of the mantle. The non-dimensional reference permeability M^* is proportional to k_{ϕ_0}/η_{melt} and expresses how easily the upward migration of magma takes place. We varied the values of M^* in the range of $5 \le M^* \le 100$, which corresponds to the change in the viscosity η_{melt} of magma by a factor of 20 (1–20 Pa s).

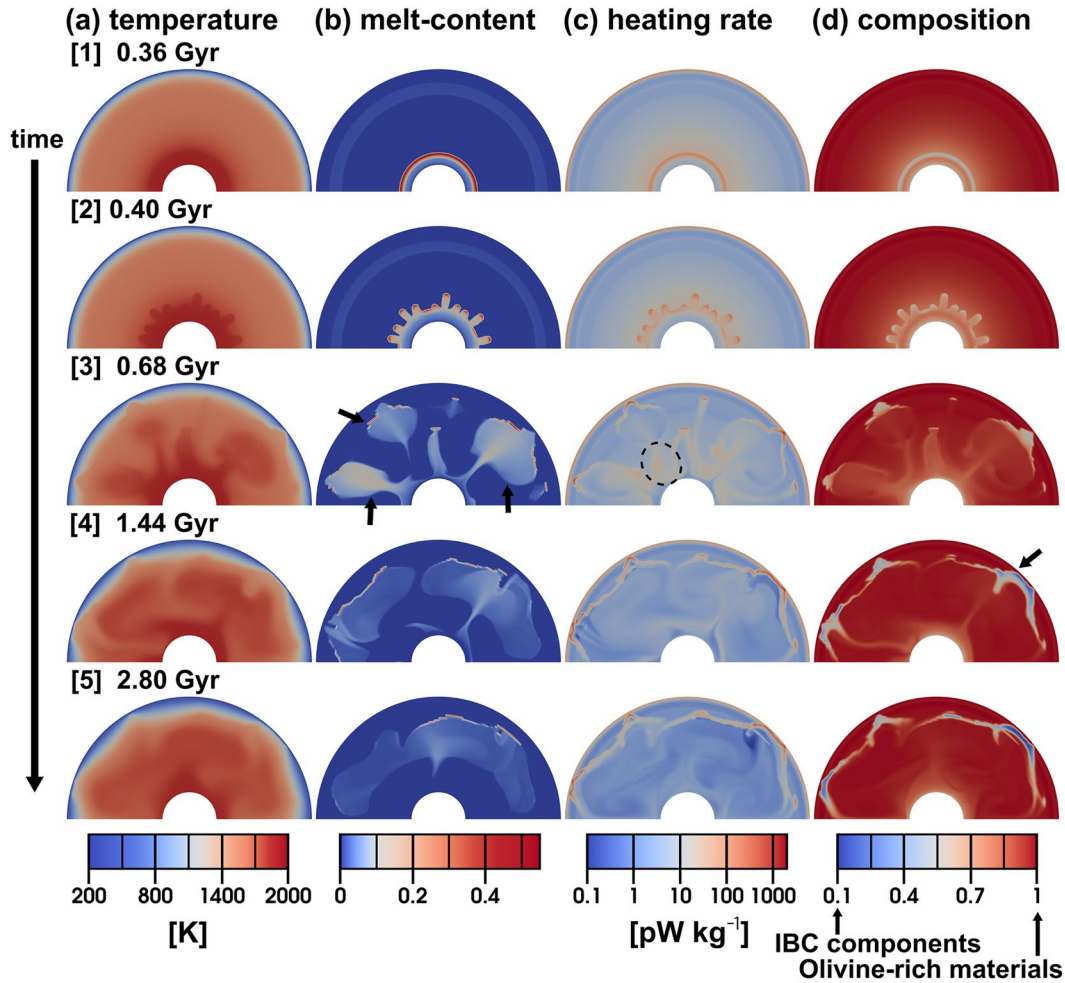

Figure 2. Snapshots of the distributions of (a) temperature T, (b) melt-content ϕ, (c) internal heating rate q, and (d) composition ξ_b calculated for Case Ref where $M^* = 100$; Ra $= 2.15 \times 10^6$, corresponding to $\eta_0 = 10^{20}$ Pa s; $E_T^* = 3$; $T_p = 1550$ K; $l^* = 4.5$; $F_{crst}^* = 8$. The elapsed times are indicated in the figure. In (d), the blue color stands for the ilmenite-bearing cumulates components, while the red color for the olivine-rich end-member. The numbers [1]–[5] correspond with those of Figure 4.

On the other hand, the Rayleigh number Ra is inversely proportional to the reference viscosity and expresses how readily mantle convection occurs. We estimated that this value is in the range of Ra $= 2.15 \times 10^4$–10^6 corresponding to $\eta_0 = 10^{22}$–10^{20} Pa s), based on an earlier estimate of mantle rheology (Karato & Wu, 1993).

Other parameters listed in Table 2 are also varied to see how the numerical results depend on the thermal and compositional structure of the mantle assumed in the initial conditions. The range of T_p is decided according to that of initial temperature in Laneuville et al. (2013) and that of post-overturn temperature in some models (Boukaré et al., 2018; H. Li et al., 2019; Yu et al., 2019). l^* is estimated from the density of the basal layer which is enriched in the overturned materials obtained by the results of previous overturn models (e.g., H. Li et al., 2019; Zhao et al., 2019). The thickness of the overturned layer is thinner and more concentrated in HPEs and the IBC components with a lower l^*. We also take the value of F_{crst}^* from the estimates in Konrad and Spohn (1997) and Spohn et al. (2001).

3. Results

3.1. The Reference Case

Figures 2 and 3 show the reference case (Case Ref) calculated at the reference permeability $M^* = 100$; the Rayleigh number Ra $= 2.15 \times 10^6$, corresponding to $\eta_0 = 10^{20}$ Pa s; the sensitivity of viscosity on temperature

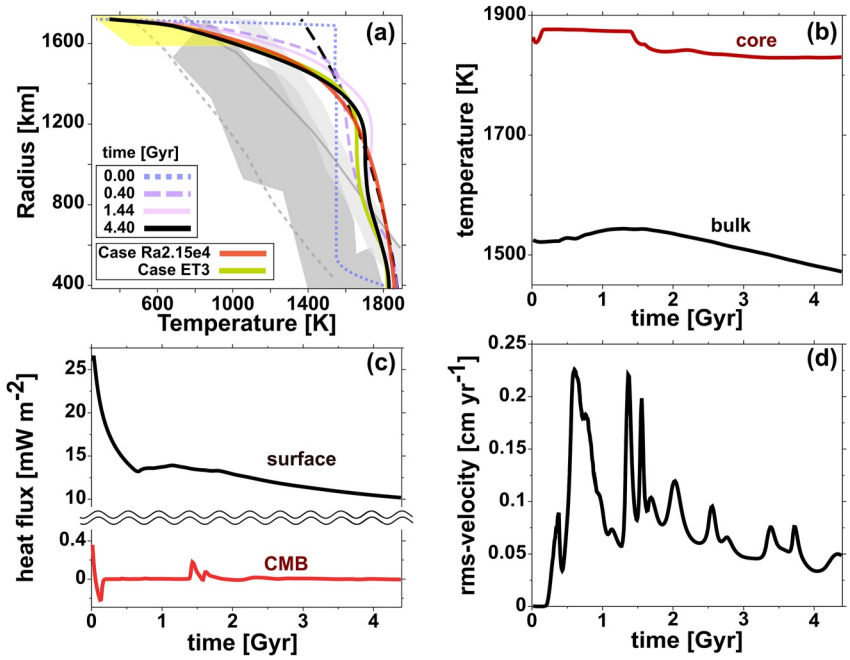

Figure 3. (a) The horizontal averages of the temperature-distributions at various elapsed times for Case Ref. Also shown are the horizontally averaged temperature at 4.4 Gyr for Case Ra2.15e4 (Ra = 2.15×10^4) and ET3 ($E_T^* = 3$). In (a), the gray and light-gray areas are the temperature distributions in today's lunar mantle inferred by Khan et al. (2006, 2014), respectively; the yellow areas are those estimated from the heat flux at the surface (Siegler & Smrekar, 2014; Siegler et al., 2022); the gray lines are those estimated under the assumption that the mantle consists of dry olivine (the solid line) and wet olivine with 0.01 wt % H_2O (the dashed line) by Karato (2013). Also shown are (b) the average temperature in the mantle (bulk) and the temperature of the core; (c) the horizontal average of heat flux on the surface and the core-mantle boundary; (d) the root-mean-square average of matrix-velocity in the mantle all plotted against time.

$E_T^* = 6$; the potential temperature $T_p = 1550$ K; the initial thickness of the overturned layer $l^* = 1/4.5$; the initial crustal fraction of the HPEs $F_{crst}^* = 8$ (Table 2).

3.1.1. Thermal and Structural Evolution of the Mantle

Figures 2 and 3 as well as the animation in (Movies S1–S5) illustrate how the mantle evolves dynamically by magmatism and mantle convection. The partially molten region in the uppermost mantle assumed in the initial condition shrinks with time owing to conductive cooling from the surface boundary (Figure 2b for 0.36–0.68 Gyr). In contrast, the temperature rises in the deep mantle that is enriched in HPEs in the initial condition, and magma is generated there within the first 150 Myr (Figures 2a and 3a; see also Movies S1–S3). The distributions of melt-content, HPEs, and bulk composition in the deep mantle are laterally uniform at the beginning of the calculated evolutionary history of the mantle (Figures 2b–2d for 0.36 Gyr). However, finger-like structures, or "melt-fingers," eventually develop along the top of the partially molten region at a depth after around 0.4 Gyr. The fingertips are enriched in HPEs and the IBC components because of their transport by upward migrating magma (Figure 2 for 0.40 Gyr). Following the development of melt-fingers, partially molten plumes develop and ascend often along the fingers (see the arrows in Figure 2b) and induce peaks in the plot of rms-velocity in Figure 3d. Most of the partially molten plumes ascend to the uppermost mantle and reach the depth levels as shallow as around 25 km by 0.7 Gyr (Figure 2b and Table 3; see also magma flux in Figure S1 of the Supporting Information S1). These plumes in the uppermost mantle gradually solidify as they are cooled from the surface boundary. Some partially molten plumes, however, solidify in the mid and deep mantle (see the dashed circle in Figure 2c for 0.68 Gyr). The solidified materials enriched in HPEs and the IBC components then sink to the deep mantle because of their compositionally induced negative buoyancy (see Figure 2d; see also Movie S4 for around 0.60 and 0.84 Gyr). Internal heating by HPEs in these materials induces further partial melting in the deep mantle. As a consequence, partially molten plumes develop until around 4 Gyr, although they become fainter with time as the HPEs decline after around 2 Gyr (2b and 3b–3d).

Some materials in the uppermost mantle are enriched in HPEs and the IBC components by partially molten plumes (Figures 2c and 2d). These materials founder into the deep mantle owing to their compositionally induced

Table 3
The Values of the Parameters Listed in Table 2 and Results

Case #	M^*	Ra	E_T^*	T_p (K)	$1/l^*$	F_{crst}^*	ΔR_{peak} (km)	$t_{\Delta R}$ (Gyr)	χ_{Gyr} (km Gyr^{-})	L_ϕ (km)
Ref	100	2.15×10^6	6	1550	4.5	8	3.00	0.66	−1.01	25
M50	50	2.15×10^6	6	1550	4.5	8	4.44	0.70	−1.33	185
M20	20	2.15×10^6	6	1550	4.5	8	6.62	0.89	−1.47	225
M5	5	2.15×10^6	6	1550	4.5	8	8.95	1.73	−1.78	200
Ra2.15e4	100	2.15×10^4	6	1550	4.5	8	3.84	1.04	−1.16	75
Ra2.15e5	100	2.15×10^5	6	1550	4.5	8	3.80	1.05	−1.17	60
Ra7.15e5	100	7.15×10^5	6	1550	4.5	8	3.53	0.83	−0.96	40
ET3	100	2.15×10^6	3	1550	4.5	8	3.06	0.78	−0.76	15
ET9	100	2.15×10^6	9	1550	4.5	8	3.30	0.66	−1.28	165
Tm1400	100	2.15×10^6	6	1400	4.5	8	3.62	1.36	−0.57	30
Tm1475	100	2.15×10^6	6	1475	4.5	8	3.34	1.13	−0.67	25
Tm1625	100	2.15×10^6	6	1625	4.5	8	3.80	0.50	−1.00	30
Tm1700	100	2.15×10^6	6	1700	4.5	8	4.23	0.42	−1.41	115
l1.5	100	2.15×10^6	6	1550	1.5	8	3.01	1.04	−1.17	190
l2.5	100	2.15×10^6	6	1550	2.5	8	3.66	0.86	−1.43	80
l3.5	100	2.15×10^6	6	1550	3.5	8	3.51	0.69	−0.97	170
l5.5	100	2.15×10^6	6	1550	5.5	8	2.92	0.85	−1.20	20
l6.5	100	2.15×10^6	6	1550	6.5	8	2.50	0.62	−0.93	15
l0	100	2.15×10^6	6	1550	0	8	0.22	1.45	−0.62	215
Fcrst4	100	2.15×10^6	6	1550	4.5	4	3.85	0.69	−1.23	25
Fcrst16	100	2.15×10^6	6	1550	4.5	16	1.69	1.07	−1.03	190
Fcrst32	100	2.15×10^6	6	1550	4.5	32	−0.50	1.46	−0.95	395
M50-Ra2.15e4	50	2.15×10^4	6	1550	4.5	8	5.25	0.79	−0.83	205
M20-Ra2.15e4	20	2.15×10^4	6	1550	4.5	8	8.91	1.35	−0.82	305
M5-Ra2.15e4	5	2.15×10^4	6	1550	4.5	8	12.21	3.36	−0.37	285
M0-Ra2.15e4	0	2.15×10^4	6	1550	4.5	8	15.32	4.40	1.21	375
M50-l5.5	50	2.15×10^6	6	1550	5.5	8	4.00	0.73	−1.22	160
M20-l5.5	20	2.15×10^6	6	1550	5.5	8	7.09	0.83	−1.12	210
M5-l5.5	5	2.15×10^6	6	1550	5.5	8	9.00	1.80	−1.25	195
Tm1400-l5.5	100	2.15×10^6	6	1400	5.5	8	3.86	1.12	−0.10	155
Tm1700-l5.5	100	2.15×10^6	6	1700	5.5	8	4.09	0.35	−1.16	40
Tm1400-l1.5	100	2.15×10^6	6	1400	1.5	8	4.91	1.68	−0.84	210
Tm1700-l1.5	100	2.15×10^6	6	1700	1.5	8	−0.21	0.53	−1.08	105
Tm1400-l5.5	5	2.15×10^6	6	1400	5.5	8	9.83	3.40	−0.13	270
Ra2.15e4-l5.5	100	2.15×10^4	6	1550	5.5	8	3.44	1.09	−1.17	25
Ra2.15e5-l5.5	100	2.15×10^5	6	1550	5.5	8	3.15	1.10	−1.17	25
M50-Ra4-l5.5	50	2.15×10^4	6	1550	5.5	8	4.98	1.15	−1.17	175
M20-Ra4-l5.5	20	2.15×10^4	6	1550	5.5	8	9.43	1.62	−0.91	310
M5-Ra4-l5.5	5	2.15×10^4	6	1550	5.5	8	12.57	3.19	−0.37	290
M5-Ra5-l5.5	5	2.15×10^5	6	1550	5.5	8	12.46	3.02	−0.19	285
ET9-l5.5	100	2.15×10^6	9	1550	5.5	8	3.28	0.60	−0.87	85
l5.5-Fcrst16	100	2.15×10^6	6	1550	5.5	16	1.74	0.890	−0.85	185

Table 3
Continued

Case #	M^*	Ra	E_T^*	T_p (K)	$1/l^*$	F_{crst}^*	ΔR_{peak} (km)	$t_{\Delta R}$ (Gyr)	χ_{Gyr} (km Gyr^{-})	L_ϕ (km)
l5.5-Fcrst32	100	2.15×10^6	6	1550	5.5	32	−0.21	1.30	−0.91	315
ET3-l5.5	100	2.15×10^6	3	1550	5.5	8	2.99	0.80	−1.03	20
ET3-l1.5	100	2.15×10^6	3	1550	1.5	8	4.00	1.11	−0.82	160
M5-ET3-l5.5	5	2.15×10^6	3	1550	5.5	8	10.40	2.34	−2.00	180
Ra4-ET3-l5.5	100	2.15×10^4	3	1550	5.5	8	3.88	1.12	−1.67	25
Ra4-ET9-l5.5	100	2.15×10^4	9	1550	5.5	8	3.00	0.66	−1.17	150
ET9-l1.5	100	2.15×10^6	9	1550	1.5	8	2.19	0.85	−1.39	160
M5-ET9-l5.5	5	2.15×10^6	9	1550	5.5	8	8.75	1.62	−1.91	185
Tm14-l5.5-Fcrst16	100	2.15×10^6	6	1400	5.5	16	2.46	1.06	0.07	225
Tm17-l5.5-Fcrst16	100	2.15×10^6	6	1700	5.5	16	2.93	0.45	−1.10	50
ET3-l5.5-Fcrst16	100	2.15×10^6	3	1550	5.5	16	1.96	0.83	−0.94	50
ET9-l5.5-Fcrst16	100	2.15×10^6	9	1550	5.5	16	1.80	0.80	−1.27	195
Ra4-l5.5-Fcrst16	100	2.15×10^4	6	1550	5.5	16	2.14	1.46	−1.10	100
Ra5-l5.5-Fcrst16	100	2.15×10^5	6	1550	5.5	16	2.06	1.58	−0.86	115
l1.5-Fcrst16	100	2.15×10^6	6	1550	1.5	16	0.83	1.45	−0.97	90
l3.5-Fcrst16	100	2.15×10^6	6	1550	3.5	16	1.88	0.98	−0.69	185
M5-l5.5-Fcrst16	5	2.15×10^6	6	1550	5.5	16	4.37	1.79	−0.71	240
M20-l5.5-Fcrst16	20	2.15×10^6	6	1550	5.5	16	3.63	1.07	−0.60	260
M50-l5.5-Fcrst16	50	2.15×10^6	6	1550	5.5	16	2.65	0.80	−1.05	205
No-conv-HPEs-Mass-tr	100	2.15×10^2	6	1550	4.5	8	−0.65	1.11	−0.71	195
No-HPEs-Mass-tr	100	2.15×10^6	6	1550	4.5	8	−4.12	0.49	−0.80	20
No-Mass-tr	100	2.15×10^6	6	1550	4.5	8	−5.01	0.55	−1.30	15
vl-change	100	2.15×10^6	6	1550	4.5	8	3.67	0.70	−1.08	65
melt-dep	100	2.15×10^6	6	1550	4.5	8	2.57	0.57	−0.71	35
melt-dep-Ra4	100	2.15×10^4	6	1550	4.5	8	6.84	0.91	−0.28	305
IBC-dep	100	2.15×10^6	6	1550	4.5	8	3.20	0.75	−0.91	20
rl-100 km	100	2.15×10^6	6	1550	4.5	8	2.45	0.68	−1.23	85
beta0202 ($\beta = 0.202$)	100	2.15×10^6	6	1550	4.5	8	5.21	0.70	−0.85	100
beta0067 ($\beta = 0.067$)	100	2.15×10^6	6	1550	4.5	8	−0.60	2.38	−0.85	20

Note. ΔR_{peak} and $t_{\Delta R}$ stand for the magnitude and timing of the peak of radial expansion, respectively; χ_{Gyr} the contraction rate for the past 1 Gyr obtained by least squares method; L_ϕ the shallowest depth levels of partially molten regions other than that in the initial state.

negative buoyancy (see the arrow in Figure 2d). The return flow of this foundering produces magma that is not enriched in HPEs and the IBC components by decompression melting (Figures 2b–2d for 1.44 Gyr; see also Movies S2–S4 for around 1.28 and 1.44 Gyr).

We will describe more about melt-fingers and partially molten plumes in Section 3.1.3, below.

3.1.2. Radius Change

Figure 4 shows how the radius changes with time owing to the mantle evolution shown in Figures 2 and 3. The radius of the Moon changes with time for two reasons, thermal expansion/contraction, and melting of the mantle (see Equation 12), as indicated by the blue and red lines in the figure, respectively. The blue line in Figure 4 shows that the Moon thermally expands by 0.4 km in the early history as the mantle is heated up and then contracts until the end of the calculation as the mantle is cooled (Figure 3b). On the other hand, the red line indicates the Moon

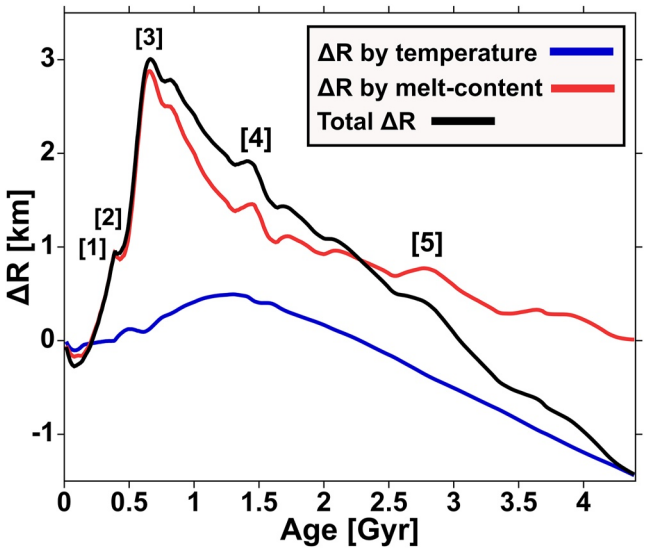

Figure 4. The history of radius change of planet calculated in the reference case (Case Ref). The radius change ΔR is defined by Equation 12; the blue and red lines indicate the contribution of thermal expansion/contraction and melting, respectively, to the total radius change (the black line). The numbers [1]–[5] correspond with those of Figure 2.

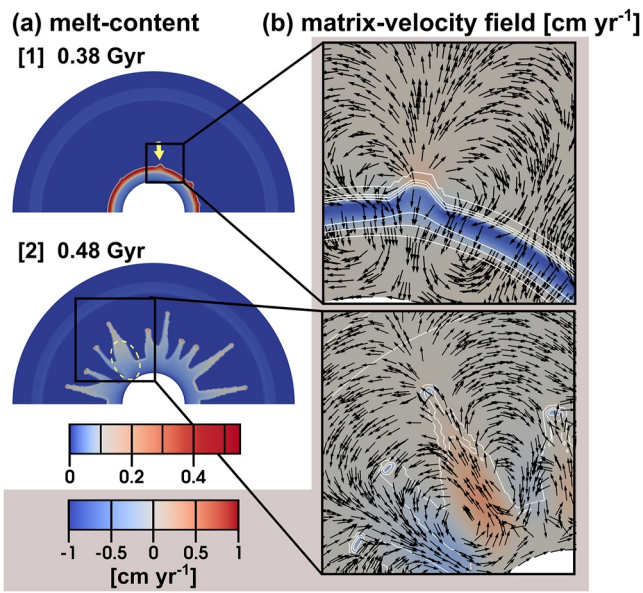

Figure 5. Snapshots of the (a) melt-content ϕ and (b) matrix-velocity field in the reference case (Case Ref). In (b), the red and blue colors show the regions where the convective flow points upward and downward, respectively; the arrows express the direction of convective flow but not its magnitude. The contour lines show the ϕ-distribution with the contour interval of 0.1 starting from 0.

expands by 3 km for the first 0.7 Gyr owing to widespread partial melting of the mantle caused by melt-fingers and partially molten plumes (the peak [3] in Figure 4). After that, the Moon gradually contracts with time as the mantle solidifies. Note that the contraction is not monotonous: slight expansion occurs several times when partially molten plumes develop (see [4] and [5] in Figures 2 and 4). As a whole, the black line in Figure 4 indicates that the Moon radially expands by about 3 km during the first 0.7 Gyr and then contracts at the rate of around -1.0 km Gyr^{-1} until the end of the calculated history (Table 3).

3.1.3. Melt-Fingers and Partially Molten Plumes

To understand why melt-fingers grow from the partially molten region at depths around 0.4 Gyr in Figures 2a and 2b, we delineate the velocity field of the matrix around a nascent finger in the frame for 0.38 Gyr of Figure 5 (see the bump indicated by the yellow arrow). This frame shows that the matrix expands around the fingertip to let it grow upward. To show why this expansion occurs, we decompose the flow field $\mathbf{U}$ into the components driven by volume change of the matrix $\mathbf{U}^{vc}$ and that driven by the buoyancy force $\mathbf{U}^{by}$ as

$$\mathbf{U} = \mathbf{U}^{vc} + \mathbf{U}^{by} \ : \tag{14}$$

we calculated $\mathbf{U}^{vc}$ from Equations 6, A1 and A2 with Ra = 0 and the original value of M^*, while $\mathbf{U}^{by}$ from these equations with $M^* = 0$ and the original value of Ra. We confirmed that the flow field $\mathbf{U}$ in Figure 5b for 0.38 Gyr is close to that of $\mathbf{U}^{vc}$, implying that the matrix expansion around the fingertip is caused by the injection of upward migrating magma; upward migration of magma with respect to the coexisting matrix is the cause of growth of melt-fingers. (We recalculated melt-fingers on a mesh with twice higher resolution and confirmed that fingers still grow; melt-fingers are not an artifact of numerical instability.)

After 100 Myr from the development of melt-fingers (Figure 5 for 0.48 Gyr), some stems of the melt-fingers become thicker with time as the fingertips migrate upward from the partially molten layer at depth (see the yellow dashed circle in the figure). In the thickened area, both the matrix and the melt migrate upward (Figure 5). We decomposed the flow field $\mathbf{U}$ (see Equation 14) and found that $\mathbf{U}$ around the stem is dominated by $\mathbf{U}^{by}$, implying that the thickened area is a partially molten plume driven by the buoyancy of the melt.

3.2. The Occurrence of Melt-Fingers and Partially Molten Plumes

To understand under what condition melt-fingers and partially molten plumes observed in the reference case grow, we calculated the model at various values of the reference permeability M^*, and the Rayleigh number Ra.

The reference permeability M^* influences the growth of melt-fingers; the snapshots of Case M5 ($M^* = 5$ and other parameters fixed at their default values) illustrate that the melt-fingers do not occur at the lower reference permeability of this case (Figure 6a); we confirmed that $\mathbf{U}^{vc}$ is negligibly small in this case. Instead of melt-fingers, partially molten plumes that are broader than those observed in the reference case rise to the depth levels of 200 km by around 1.7 Gyr (Figure 6a for 1.72 Gyr and Table 3). The plumes laterally extend and form a continuous layer of partially molten materials (Figure 6a). The partially molten layer then solidifies upon cooling from the surface boundary; the layer, however, still remains in the mid-mantle at 4.4 Gyr (Figure 6a). We observed that melt-fingers grow only in the cases calculated at $M^* \geq 50$ (see Figure S2 in Supporting Information S1).

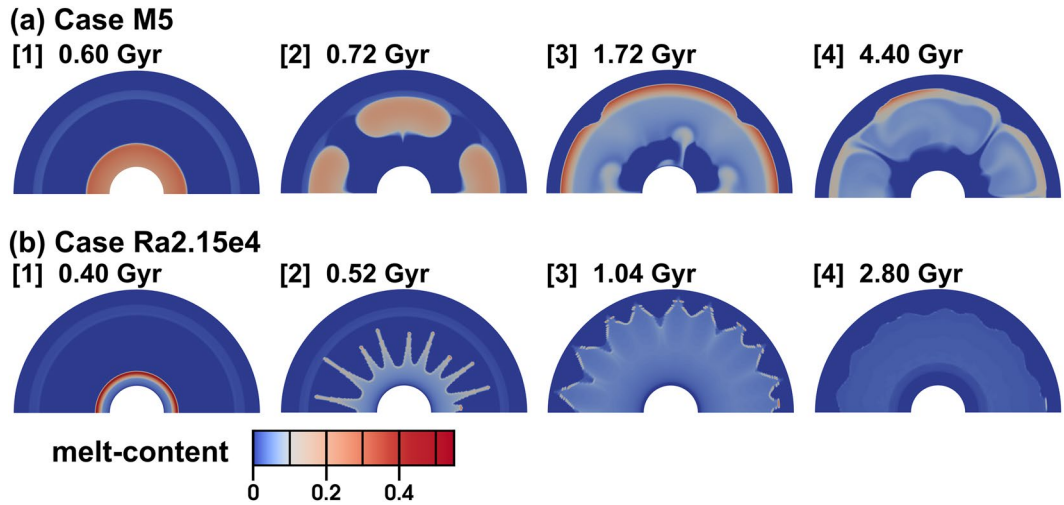

Figure 6. Snapshots of the distributions of melt-content ϕ calculated in cases with (a) a reduced reference permeability (Case M5) and (b) a reduced Rayleigh number (Case Ra2.15e4). The numbers [1]–[5] correspond with those of Figures 14a and 14e.

At $M^* = 100$, we also calculated several models at various values of Ra in the range from 2.15×10^2 to 2.15×10^6 (Table 3); we found that melt-fingers develop regardless of the values of Ra, implying that buoyancy does not play any role in the growth of melt-fingers (Figure 6b). This result reinforces the above conclusion that melt-fingers develop because of matrix expansion around fingertips (Section 3.1.3).

We further calculated Case No-conv-HPEs-Mass-tr where the convection is sluggish ($\mathrm{Ra} = 2.15 \times 10^2$) and transport of HPEs and the IBC components is negligible: the partition coefficient of HPEs D is 1 (see Equation A11 in Appendix A), and the model starts from a compositionally uniform mantle with the bulk composition of $\xi_b = \xi_e$. We found that melt-fingers develop even in this case, implying that the development of melt-fingers does not depend on these parameters.

In contrast to melt-fingers, the growth of partially molten plumes depends on the Rayleigh number. At $\mathrm{Ra} = 2.15 \times 10^4$ that is lower than Ra of the reference case by a factor of 100 (Case Ra2.15e4), only melt-fingers develop, and partially molten plumes do not grow (Figure 6b); we confirmed that $\mathbf{U}^{\mathbf{by}}$ is negligibly small in this case. Melt-fingers then grow upward to the depth level of around 75 km by around 1.0 Gyr (Figure 6b and Table 3) and then expand laterally, to make the most part of the mantle partially molten (Figure 6b for 1.04 Gyr). After that, the partially molten region shrinks monotonously with time owing to conductive cooling from the surface boundary (Figure 6b for 2.80 Gyr). We found that partially molten plumes grow only in the cases calculated at $\mathrm{Ra} \geq 7.15 \times 10^5$ (see Figure S3 in Supporting Information S1). This result reinforces that partially molten plumes are driven by their buoyancy.

The melt-fingers observed here are different from the pencil-shaped upwellings reported by Whitehead and Luther (1975) despite the similarity of shape. These upwellings develop when there is a viscosity contrast between the upwellings and the surrounding fluid, whereas our melt-fingers grow even when there is no viscosity contrast.

3.3. The Effects of More Sophisticated Rheology

In the cases described above, we assumed that the viscosity of the mantle depends only on the temperature (see Equation 11) for simplicity. However, some earlier studies show that the viscosity depends on the contents of melt and the IBC components. In this section, we considered the reduction of viscosity by melting (e.g., Hirth & Kohlstedt, 2003; Mei et al., 2002; Scott & Kohlstedt, 2006) and the IBC components (e.g., Dygert et al., 2016; H. Li et al., 2019; N. Zhang et al., 2017). The viscosity depends on the melt-content ϕ and the ratio of the olivine-rich materials to the IBC components $F_{ol} = (\xi_b - \xi_e)/(1 - \xi_e)$ as well as the temperature as

$$\eta = [F_{ol}\eta_0 + (1 - F_{ol})\eta_{IBC}]\exp\left[E_T(T_{ref} - T) - \alpha_\phi \phi\right], \quad (15)$$

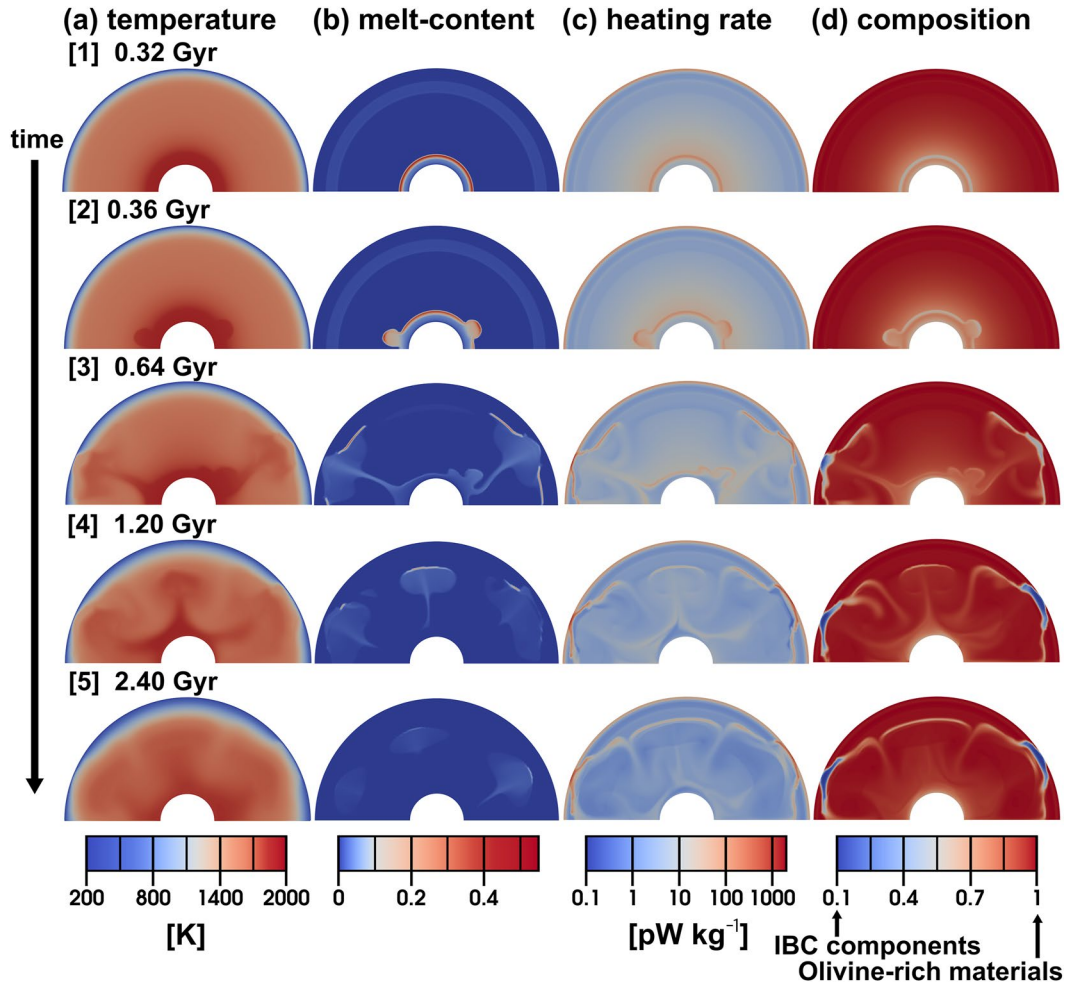

Figure 7. The same as Figure 2 but for Case melt-dep, where viscosity reduction by melting is considered.

where, $\alpha_\phi = 26$ is the melt-weakening factor (Mei et al., 2002), and the viscosity reduction by melting is truncated at its value at $\phi = 0.4$; $\eta_{IBC} = 7.5 \times 10^{18}$ Pa s is the viscosity of the IBC components (Dygert et al., 2016). Note that F_{ol} depends on the composition ξ_b, which changes with time by magmatism. We calculated two cases where the ϕ-dependent viscosity ($F_{ol} = 1$ is assumed in Equation 15; Case melt-dep) and the IBC-dependent viscosity ($\alpha_\phi = 0$ is assumed in Equation 15; Case IBC-dep) are considered.

Figures 7 and 8 where the results of Case melt-dep are presented show that the effects of ϕ-dependent viscosity do not significantly affect the overall features of mantle evolution observed for Case Ref. The partially molten region in the deep mantle vertically extends at the beginning of the calculated history of the mantle (Figure 7 for 0.32 Gyr). Partially molten plumes then develop at the top of the partially molten region (Figure 7 for 0.36 Gyr) and rise to the uppermost mantle. The plume activity continues over billions of years (Figure 7 for 0.64–2.40 Gyr). In this case, the Moon expands by 2.6 km for the first several million years and then contracts at the rate of around -0.7 km Gyr^{-1} until the end of the calculated history (Figure 8). These overall features are the same as those observed for Case Ref.

However, melt-fingers observed for Case Ref do not grow in this case. To clarify the reason for the absence of melt-fingers, we decomposed the flow field $\mathbf{U}$ around the partially molten bump in Figure 9b into the components driven by volume change of the matrix $\mathbf{U}^{vc}$ and that driven by buoyancy force $\mathbf{U}^{by}$ as we did in Section 3.1.3 of the main article and found that $\mathbf{U}^{by} \gg \mathbf{U}^{vc}$ holds. $\mathbf{U}^{by}$ represents the rotation of matrix within the bump observed in the figure. This rotation is enabled by the reduction in viscosity along the head of the bump that accommodates the strong shear caused by the rotational flow. The strong buoyancy-driven flow $\mathbf{U}^{by}$ overshadows $\mathbf{U}^{vc}$ that induces a melt-finger.

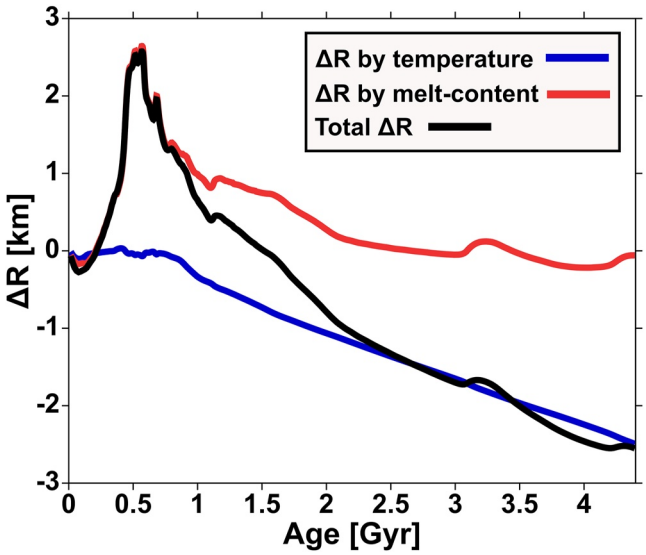

Figure 8. The same as Figure 4 but for Case melt-dep.

In contrast, we found no conspicuous effects of the IBC-dependent viscosity on numerical results in Case IBC-dep: the overall features of the mantle evolution observed in the reference case were not affected by the IBC-dependent viscosity, and both melt-fingers and partially molten plumes developed as in the reference case. The effects of the IBC-dependent viscosity are negligible in our study because the viscosity variation by this dependence is only an order of magnitude at most for the variation in the content of the IBC components realized in the numerical models.

3.4. The Effects of Density Inversion Between Melts and Matrix

The density of the solid phase with $\xi_s = 1$ is always denser than that of the melt phase with $\xi_l = 0.1$ in the cases described so far (see Equations 2 and 3, and the red line in Figure 10a). This occurred because we estimated $\Delta v_l / v_0$ in Equation 3 from the solidus curve of lunar mantle materials (Garcia et al., 2011, 2012; Katz et al., 2003). (see Equations 9 and 10 and Figure 10b as well as the assumed values of $\Delta\rho_\infty/\rho_0 = 0.005$, $\Delta\rho_{zero}/\rho_0 = 0.22$, and $\lambda = 16.42$ GPa in Equation 5.) However, some studies suggest that IBC-rich magma can be denser than the coexisting matrix in the deep mantle of the Moon (e.g., Sakamaki et al., 2010; van Kan Parker et al., 2012; Xu et al., 2022). To see how this possible density inversion affects our numerical results, we calculated the two additional cases (vl-change and beta0202). In Case vl-change, which is calculated at $\rho_\infty/\rho_0 = 0.002$, $\Delta\rho_{zero}/\rho_0 = 0.35$, and $\lambda = 4.56$ GPa (see Equation 5), melt phase is denser than that of the coexisting at radius r less than around 800 km (see the blue line and P_1 in Figure 10a). Note that this change in parameter values slightly raises the solidus temperature as shown in Figure 10b. To see if this higher solidus temperature affects our numerical results in Case vl-change, we also calculated Case beta0202 (see the black line in Figure 10a), where β is 0.202 (the density of IBC (end-member B) is 3,965 kg m^{-3}) but the default values are assumed for $\Delta\rho_\infty/\rho_0$, $\Delta\rho_{zero}/\rho_0$, and λ.

Figures 11 and 12 where the results of Case vl-change are presented show that the effects of density inversion between melts and coexisting matrix do not significantly affect the overall features of mantle evolution observed for Case Ref (see also Movies S6–S10). For the first few hundred million years, magma generated in the deep mantle sinks to the core-mantle boundary (CMB), making the mantle more enriched in HPEs and the IBC components at its base (Figure 11 for 0.52 Gyr). Partially molten plumes, however, eventually grow along the top of the partially molten region and ascend to carry the enriched materials at the base of the mantle to the uppermost mantle over billions of years (Figure 11 for 0.64–2.16 Gyr). The Moon radially expands by 3.7 km during this time (see Figure 12). The plume activity then declines with time owing to cooling of the mantle (Figure 11 for 2.16–4.00 Gyr) and the Moon accordingly contracts at a rate of 1 km Gyr^{-1}. These overall features are the same as those observed in Case Ref. (Note, however, that melt-fingers observed in Case Ref do not grow in this case because of the density inversion. The absence of melt-fingers does not affect the overall evolutionary history.)

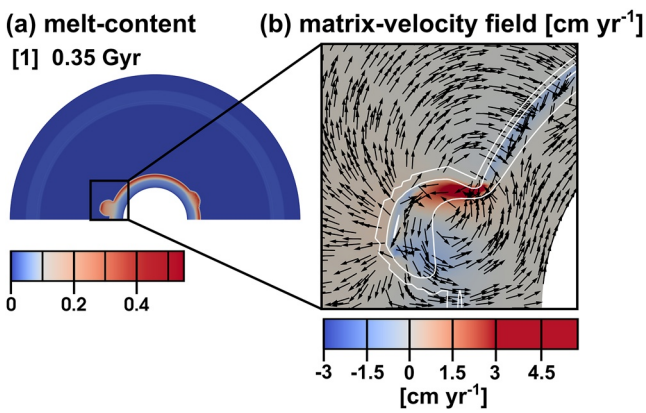

Figure 9. The same as Figure 5 but for Case melt-dep. In (b), the red and blue colors show the regions where the convective flow points upward and downward, respectively; the arrows express the direction of convective flow but not its magnitude. The contour lines show the ϕ-distribution with the contour interval of 0.2 starting from 0.

We found that the overall features of mantle evolution calculated in Case beta0202 are also the same as those calculated in Case vl-change. The slight difference in the solidus curve shown in Figure 10b does not influence the numerical results.

It may look counterintuitive that the partially molten regions in the deep mantle eventually migrate upward as partially molten plumes despite the density inversion between melts and the coexisting matrix there. This density inversion does not influence the overall upwelling flow, because melting of the mantle always causes a decrease in the bulk density (see Movie S10); the density inversion just lets magma migrate downward within upwelling partially molten plumes in the deep mantle.

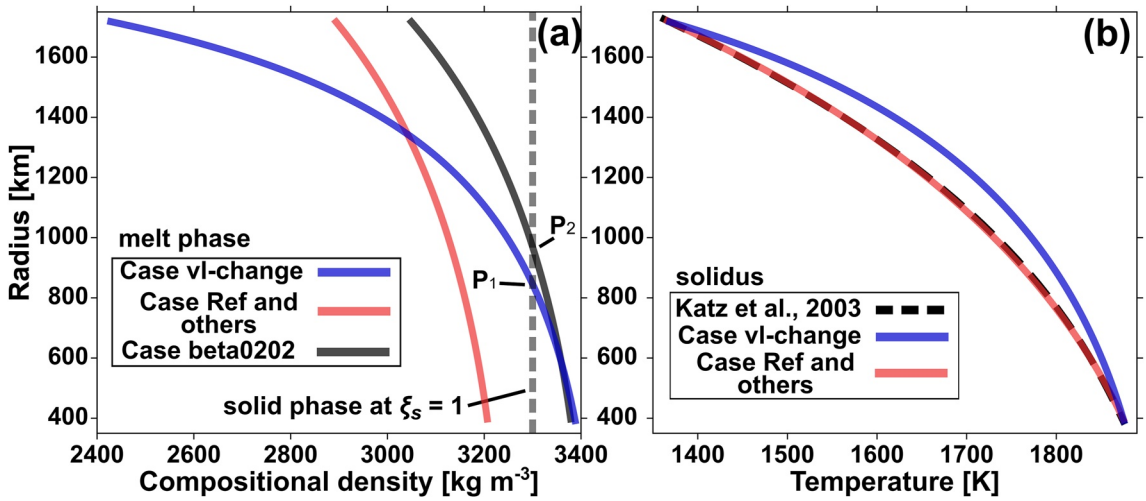

Figure 10. An illustration of (a) the density of melt phase with $\xi_1 = 0.1$, and (b) the solidus assumed in Case vl-change where the density inversion between solid and melt phases is considered. In (a), the density difference between the solid phase and the melt phase is generally consistent with that suggested by some experimental studies (van Kan Parker et al., 2012; Xu et al., 2022). In (b), the black dashed line is the solidus curve for the lunar mantle materials (Garcia et al., 2011, 2012; Katz et al., 2003).

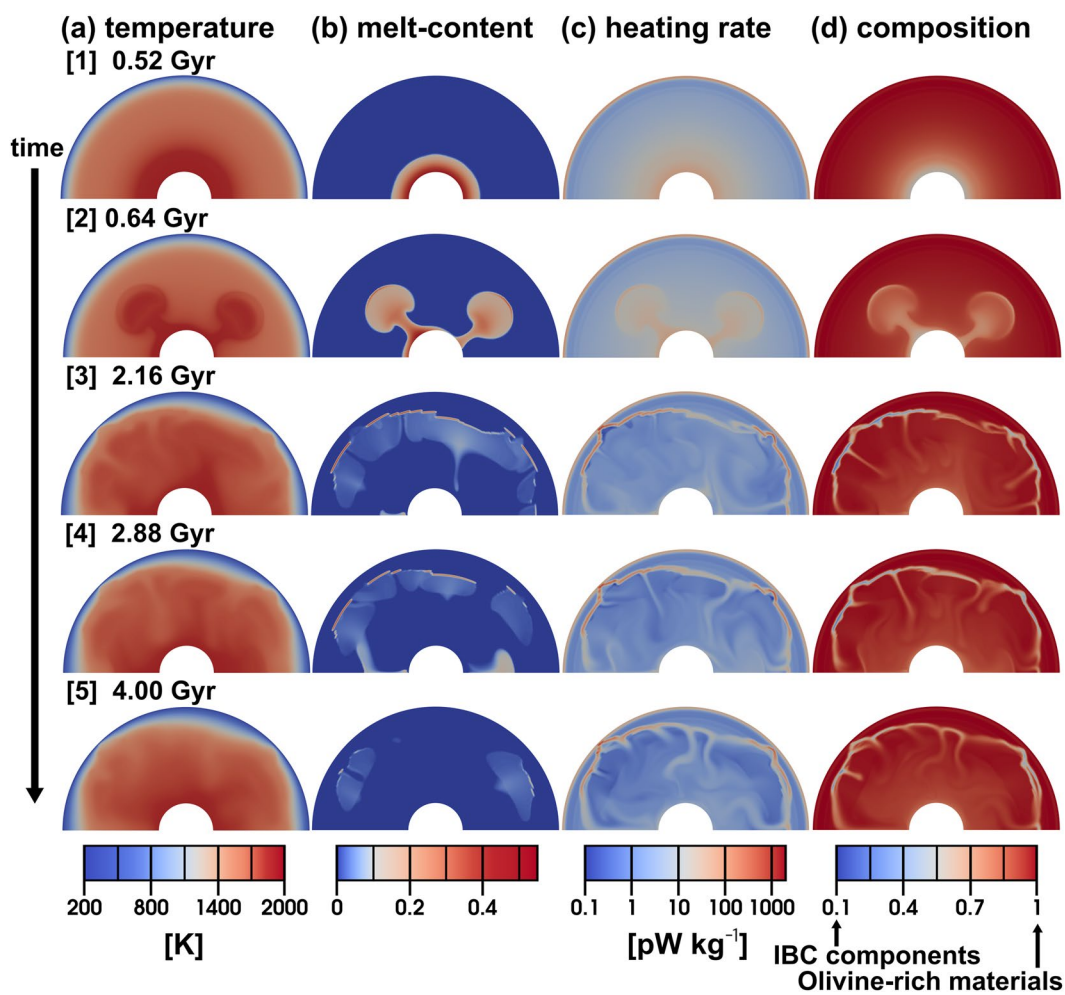

Figure 11. The same as Figure 2 but for Case vl-change, where the magma generated in the deep mantle is denser than the coexisting matrix.

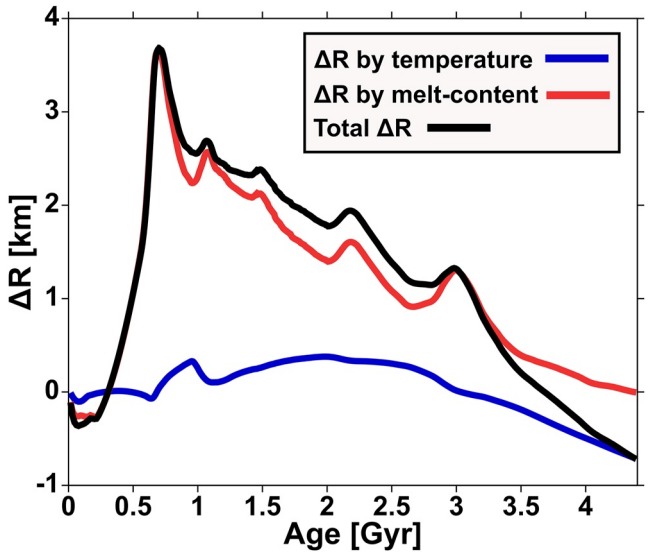

Figure 12. The same as Figure 4 but for Case vl-change.

3.5. The Effect of the Initial Distribution of Mantle Composition

To see how plume magmatism continues for billions of years in the reference case (Figure 2), we further calculated Case No-Mass-tr where we assumed a compositionally uniform mantle with the bulk composition $\xi_b = \xi_e$ in the whole mantle (Table 3). In this case, most of partially molten plumes ascend to the uppermost mantle by around 0.8 Gyr, and plume activity declines after that (Figure 13). The early decline of plume activity results from the early extraction of HPEs from the deep mantle where magma is mostly generated. In contrast, HPE-extraction by early plume magmatism is not so efficient in the reference case where the deep mantle is assumed to be enriched in the dense IBC components in the initial condition (see Section 3.1.1). The duration time of plume activity depends on the initial distribution of the dense IBC components.

3.6. Dependence of Radial Expansion on Model Parameters

We further carried out numerical experiments to show how the radial expansion-history depends on the model parameters: the reference permeability M^*; the Rayleigh number Ra; the sensitivity of viscosity to temperature E_T^*; the potential temperature T_p; the thickness of the overturned layer l^*; the initial concentration ratio of the HPEs in the crust to the mantle F_{crst}^* (Figure 14 and Table 3).

Among the parameters, the reference permeability M^* influences the expansion-history most strongly (Figure 14a); a lower M^* leads to a later peak of expansion with a larger amplitude. The larger expansion is due to a more slowly migrating magma that retains HPEs in the deep mantle for a longer period, and it allows more heat to build up in the mantle (see Figure 6a and Table 3).

The initial ratio of HPE-concentration in the crust to that in the mantle F_{crst}^* also substantially influences the magnitude of radial expansion (Figure 14b); a higher F_{crst}^* reduces radial expansion because the mantle is more depleted in HPEs and less magma is generated in the deep mantle.

The potential temperature T_p affects the timing and, to some extent, the amplitude of radial expansion as shown in Figure 14c. A higher T_p leads to an earlier peak of expansion because it implies an earlier generation of partially molten regions in the deep mantle and an earlier extension of the regions into the uppermost mantle. A higher T_p also leads to a slightly larger amplitude of the early expansion at T_p above 1550 K (Figure 14c). At this high T_p, the magma is generated immediately in the deep mantle and spreads into the uppermost mantle before most of an initial partially molten layer in the uppermost mantle is not completely cooled. The contraction due to solidification of the initial melt is smaller, and the earlier expansion becomes larger.

The thickness of the overturned layer l^* has an effect on the beginning of radial expansion (Figure 14d). A higher $1/l^*$ where the deep mantle is more enriched in HPEs induces an earlier beginning of the expansion. Note that in Case l0 where HPEs and the composition ξ_b are uniform in the whole mantle ($1/l^* = 0$), the amplitude of

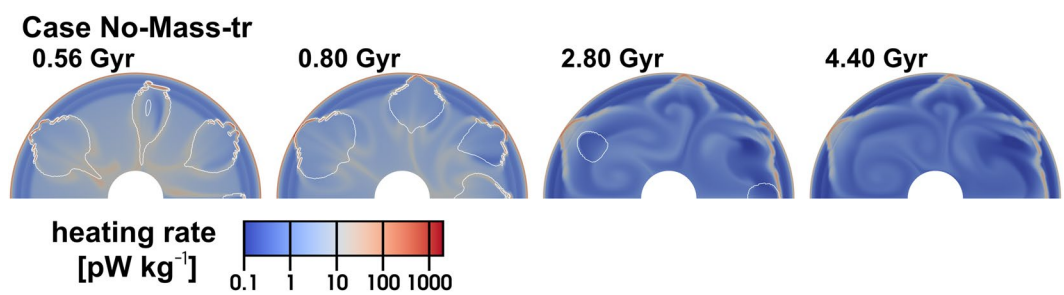

Figure 13. Snapshots of the distributions of internal heating rate q calculated in a case where the composition ξ_b is kept uniform with the eutectic composition ξ_e (Case No-Mass-tr). The contour lines show the distribution of melt-content with contour level of 0 and 0.1.

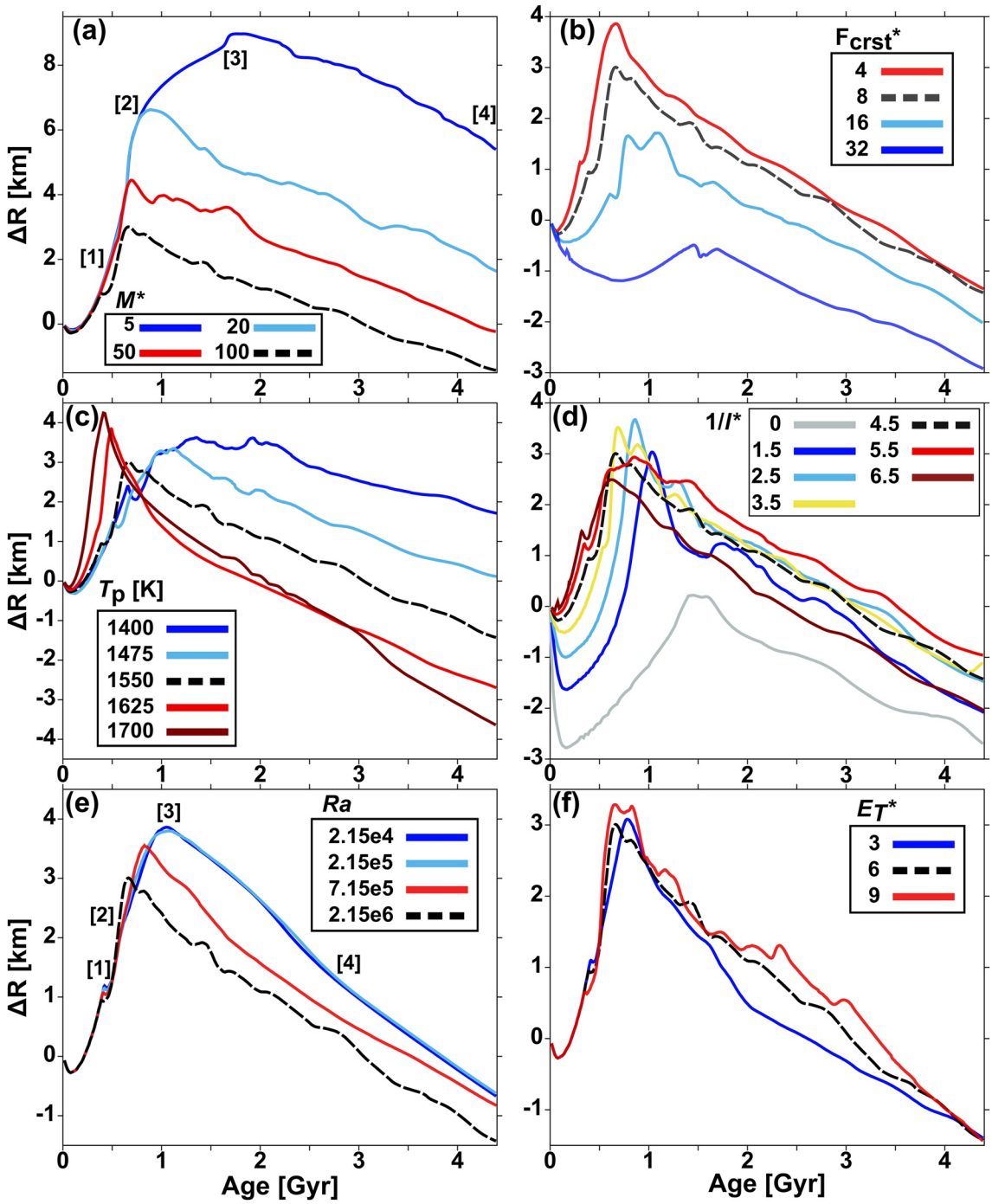

Figure 14. Plots of radius change against time calculated at various values of (a) the reference permeability M^*, (b) the initial crustal fraction of the heat-producing elements $F_{crst}{}^*$, (c) the potential temperature T_p, (d) the thickness of the overturned layer l^*, (e) the Rayleigh number Ra, and (f) the sensitivity of viscosity to temperature E_T^*. The dotted lines show the reference case (Case Ref) presented in Figures 2–4. In (a) and (e), the numbers [1]–[5] correspond with those of Figures 6a and 6b, respectively.

radial expansion is smaller than in cases where the overturned layer is considered (Figure 14d). This is because enough magma generation does not occur to cause the early expansion in Case l0. (Case l0 is different from Case No-HPEs-Mass-tr where the initial HPE-distribution is preserved throughout the calculated history (the same as Case No-conv-HPEs-Mass-tr, but Ra = 2.15×10^6). HPE-distribution is assumed to be uniform in the initial condition but becomes heterogeneous by magma-transport in Case l0.)

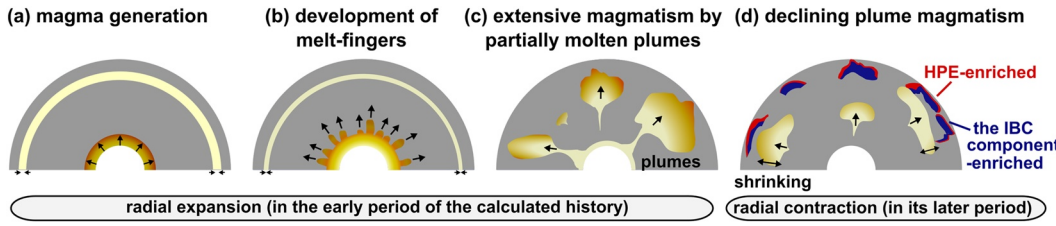

Figure 15. An illustration of the thermal and structural history of the lunar mantle inferred from our numerical study (Case Ref). The yellow color stands for melting.

Conversely, although the horizontal averages of the temperature-distributions depend on the values of Ra and E_T^* (Figure 3a), the dependences of expansion-history on the Rayleigh number Ra and the sensitivity of viscosity to temperature E_T^* are negligible as shown in Figures 14e and 14f.

4. Discussions

Figure 15 illustrates how the mantle evolves in the reference case shown in Figures 2–5. The partially molten region in the uppermost mantle shrinks with time, whereas that in the deep mantle expands on the earliest stage of the calculated history (Figure 15a). Melt-fingers then develop along the top of the partially molten region at depth, and the fingers extend upward (Figure 15b). After the growth of those, partially molten plumes driven by melt buoyancy rise to the uppermost mantle to cause plume magmatism (Figure 15c). The Moon expands in the stage of Figures 15a–15c because of melting of the mantle. These partially molten plumes transport HPEs and the IBC components from the deep mantle to the uppermost mantle. The plume magmatism then declines with time after around 2 Gyr of the calculated history because of the depletion of HPEs in the deep mantle (Figure 15d). In the latter period of the calculated history, the Moon gradually contracts by cooling and solidification of the partially molten mantle. The reference case fits in best with the observed history of the Moon among the models calculated here as we will discuss in Section 4.2.

4.1. Comparisons With Earlier Models

4.1.1. The Mantle Evolution Caused by Magmatism and Convection

A comparison with earlier classical 1-D models of lunar thermal history in the literature shows the crucial role that heat transport by migrating magma and mantle convection plays in the reference case. In earlier 1-D models where only internal heating and thermal conduction are considered, the temperature in the deep mantle monotonously increases to the solidus temperature due to internal heating, while the lithosphere monotonously thickens with time owing to cooling from the surface boundary throughout the calculated history (e.g., Solomon & Chaiken, 1976; Solomon & Toksöz, 1973; Toksőz & Solomon, 1973; Wood, 1972). These models show that the deep mantle becomes extensively molten and the lithosphere becomes as thick as around 600 km at present. In our reference case where heat transport by migrating magma and mantle convection is also considered, however, the temperature is below the solidus in most part of the deep mantle, and the thickness of the lithosphere is by less than around 350 km at 4.4 Gyr (Figure 3a).

A comparison with earlier 2- or 3-D models of the lunar thermal history where mantle convection also is considered, on the other hand, shows the crucial roles that magma plays in heat transport in the convecting mantle. The vigor of thermally driven mantle convection is controlled by the distance from the threshold for the onset of thermal convection on the plane of the Rayleigh number Ra_d and the viscosity contrast $\eta_{\mathrm{top}}/\eta_{\mathrm{bot}}$ shown in Figure 16 (Yanagisawa et al., 2016). As shown in the figure, our reference case (Case Ref) is calculated under the condition that thermally driven mantle convection is more sluggish than that of the earlier models of lunar mantle convection Z-E100, Z-E200 (N. Zhang et al., 2013a), and Zi-M650 (Ziethe et al., 2009). The lithosphere at 4.4 Gyr in our reference case is (see the black line in Figure 3a), however, thinner than that in these models (see e.g., Figure 3c in N. Zhang et al. (2013a)). Even in the models where thermally driven mantle convection does not occur at all (Case Ra2.15e4), the lithosphere (see the red line in Figure 3a) is substantially thinner than that in the earlier models KS-S (Konrad & Spohn, 1997; Spohn et al., 2001) and Ln (Laneuville et al., 2013). These differences arise because, in our models, the uppermost mantle is kept hot by melt-fingers and partially molten plumes rather than totally solid plumes. Heat transport by melt-fingers and partially molten plumes is an essential part of our models. (Note that even the lithosphere of 1-D spherically symmetric mantle of an earlier model where heat transport by migrating magma

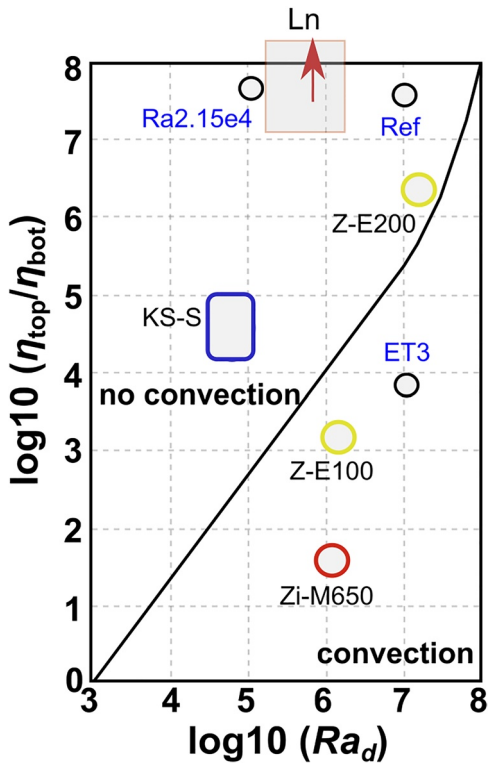

Figure 16. Plots of the critical Rayleigh number for onset of thermal convection in the 3-D spherical mantle heated from the core-mantle boundary (CMB), taken from Figure 8b in Yanagisawa et al. (2016). The viscosity is assumed to depend on the temperature and the sensitivity of the dependence is measured by the viscosity contrast between the surface boundary η_{top} and the CMB η_{bot}. Z-E100 and Z-E200 (the yellow circles) correspond to the case H50E100v5e20 and H50E200v5e20 of N. Zhang et al. (2013a); the brown arrow (Ln) by Laneuville et al. (2013); the red circle (Zi-M650) by the case M650 of Ziethe et al. (2009); the blue rounded rectangle (KS-S) by Konrad and Spohn (1997) and Spohn et al. (2001). The black circles (Ref, Ra2.15e4, and ET3) also correspond to the Case Ref, Ra2.15e4, and ET3. Note that some models in this figure use the Arrhenius law for the temperature dependence, rather than the exponential (Frank-Kamenetskii) dependence considered in our study. The difference is not important in the convecting part of the mantle beneath the stagnant lid.

is considered (U et al., 2022) is already thinner than that of the earlier models (Konrad & Spohn, 1997; Laneuville et al., 2013; Spohn et al., 2001). For a more quantitative estimate of the contribution of heat transport by melt-fingers and partially molten plumes to thinning of the lithosphere, further calculations in a 3-D spherical mantle are necessary.)

In order to understand the evolution of the compositionally stratified mantle predicted from the hypotheses of the magma ocean and mantle overturn, mass transport by migrating magma and magma-driven convective flow of the mantle is indispensable. The lunar mantle is expected to have been compositionally stratified with a layer enriched in the compositionally dense IBC components at the base of the mantle after putative crystal fractionation in the magma ocean and subsequent mantle overturn (e.g., Elkins-Tanton et al., 2011; Hess & Parmentier, 1995; Snyder et al., 1992). Some mantle convection models suggest that the basal layer eventually rises as upwelling plumes owing to its thermal buoyancy as the layer is heated by HPEs (e.g., Stegman et al., 2003; N. Zhang et al., 2017; W. B. Zhang et al., 2022; Zhong et al., 2000). In these models, however, the excess compositional density of the basal layer with respect to the overlying olivine-rich mantle is less than that suggested by some recent models of lunar mantle overturn (e.g., Yu et al., 2019; Zhao et al., 2019), greater than 160 kg m^{-3} (see Figure 6 in H. Li et al. (2019)). At this large compositional density contrast, the basal layer is convectively stable and does not ascend as solid plumes by thermal buoyancy alone, as inferred from earlier laboratory experiments of mantle convection (see Figure 1 in Le Bars and Davaille (2004)). Although the compositional density contrast in our reference case ($l^* = 4.5$) is around 180 kg m^{-3} (Figure 1), a large fraction of the IBC-rich materials in the layer is extracted and transported to the uppermost mantle by melt-fingers and by partially molten plumes driven by melt buoyancy (Figure 2); mass transport by migrating magma and magma-driven convective flow of the mantle are crucial for understanding the structural evolution of the mantle.

Our model also shows that a careful modeling of HPE transport is important to correctly understand the thermal and volcanic history of lunar mantle. The lunar volcanism has continued until 1–2 Gyr ago (e.g., Hiesinger et al., 2000; Whitten & Head, 2015), and some earlier mantle convection models conclude that the volcanism has continued for such a long period because partially molten regions remained in the cooling mantle for billions of years (Konrad & Spohn, 1997; Spohn et al., 2001; Ziethe et al., 2009). In models where the uppermost mantle is locally more enriched in HPEs, the partially molten regions observed in there persist for more than 3 Gyr (Laneuville et al., 2013, 2014, 2018). Volcanism, however, extracts HPEs from the mantle leading to the decline of subsequent volcanic activity (Cassen & Reynolds, 1973; Cassen et al., 1979; Ogawa, 2014, 2018a). In particular, Ogawa (2018a) suggests that partially molten regions disappear within 2 Gyr since the beginning of the calculated history, too short to be a model of the lunar mare volcanism, owing to the extraction of HPEs by magmatism. In our models, in contrast, magmatism continues for a much longer time despite that HPE transport by magma is considered (Figures 2 and 3) because a compositionally dense IBC-enriched layer is assumed at the base of the mantle in the initial condition. When HPE- and IBC-enriched materials in the basal layer are transported by melt-fingers and partially molten plumes, the magma often solidifies on the way to the surface and sinks again to the deep mantle (Figure 2; see also Movies S1–S5). The initial mantle stratification is necessary for magmatism to continue long. Indeed, in Case No-Mass-tr where the composition ξ_b is kept uniform ($\xi_b = \xi_e$), the mantle becomes completely solid, and magmatism declines much earlier than that in the reference case (Figure 13).

Because of the explicit implementation of a model of magma generation and migration into that of mantle convection, our models allow us to infer volcanic history directly from the calculated history of mantle melting. Earlier models have discussed volcanic history based on the calculated distribution of partially molten regions, especially the depth of the top of the regions and the calculated rate of magma generation in the

mantle (e.g., Laneuville et al., 2018; Solomon & Toksöz, 1973; Spohn et al., 2001; U et al., 2022; Wieczorek & Phillips, 2000; Wood, 1972). These models assume that the magma ascends from partially molten regions as deep as 200–800 km to the crust. However, it is not clear if magma eruption is well correlated with the depth and magma generation rate. Magma may not be able to make its way to the surface when the stress state in the lithosphere is horizontally compressive and hence when the Moon is contracting (Solomon, 1986; Solomon & Head, 1979). In our models, in contrast, magma rises directly to the base of the crust by melt-fingers and partially molten plumes (Figures 2 and 3). Several issues, however, still remain on magma migration in the crust and the uppermost mantle. It is unclear how mare basaltic magma can ascend through the crust that is not denser than the magma (e.g., Head & Wilson, 1992). The detail of formation of dikes in the uppermost mantle is also important for understanding the magma ascent (e.g., Head & Wilson, 2017; Wilson & Head, 2003, 2017). These issues may be important for also constructing a more refined model of thermal history of the Moon as noted by Lourenço et al. (2018): the thermal history can depend on the ratio of extrusive to intrusive volcanism, which can substantially depend on the porosity, thickness, and density of the crust (e.g., Head & Wilson, 2020; Morota et al., 2009; Solomon, 1975; Taguchi et al., 2017). In future studies, a more refined modeling of magma migration through the crust and the mantle is needed. (As we have already described in Section 2 above, the possible density inversion between the solid phase and the melt phase in the mantle does not affect the overall features of mantle evolution; see Section 3.4.)

For a more realistic simulation of the evolution of lunar mantle, it is essential to extend the model to a 3-D spherical shell (e.g., Laneuville et al., 2013; N. Zhang et al., 2017). 2-D annular models of mantle convection tend to predict a higher average temperature in the mantle than 3-D spherical models do, especially when the core size is small, as is the case for the Moon (Guerrero et al., 2018). Although it is computationally challenging, modeling magma generation and migration in a 3-D spherical mantle is a promising avenue for future research.

The crustal dichotomy between nearside and farside is also a long-standing issue in studies of mantle dynamics in the Moon (e.g., Cho et al., 2012; Jolliff et al., 2000; Lawrence et al., 2000). Some studies suggest that the lunar dichotomy is caused by an exogenous agent, such as the South Pole-Aitken impact (e.g., Arai et al., 2008; Jones et al., 2022; N. Zhang et al., 2022). In the future study of 3-D spherical mantle, it is important to assume the initial condition in which the uppermost mantle in the nearside is more enriched in HPEs than that in the farside (Laneuville et al., 2013, 2014, 2018; Wieczorek & Phillips, 2000).

4.1.2. The Radial Expansion/Contraction

Our reference case shows that the volume change of the mantle by melting is a key for understanding the radius change of the mantle. To cause the observed early expansion of the Moon, classical earlier models suggest that the initial temperature in the deep mantle was less than 1200 Kirk & Stevenson 1989; Solomon, 1986; Solomon & Chaiken, 1976). This upper limit is, however, substantially lower than that expected from earlier models of mantle overturn that start from giant-impact hypotheses in the literature (e.g., Canup, 2004; Lock et al., 2018; Pritchard & Stevenson, 2000). These overturn models suggest that the initial temperature in the deep mantle is approximately 1800–1900 K (e.g., Boukaré et al., 2018; Elkins-Tanton et al., 2011; Hess & Parmentier, 1995; H. Li et al., 2019). When such a high initial temperature is assumed, the early expansion occurs only nearside (Laneuville et al., 2013) or is much smaller than the observed expansion (N. Zhang et al., 2013a). In a model where the blanket effect in the crust is taken into account (Ziethe et al., 2009; N. Zhang et al., 2013b), thermal expansion of more than 1 km does occur but continues for longer than 1 Gyr, too long to account for the radial expansion of the Moon (e.g., Andrews-Hanna et al., 2013); the thermal expansion continues for such a long period even in our reference case, as shown by the blue line in Figure 4. In our model, however, global expansion occurs by a few kilometers within the first 0.7 Gyr of the calculated history because of melting of the mantle. The radial expansion by melting occurs earlier and is larger than the thermal expansion (Figure 4), suggesting that mantle melting dominates the radial expansion/contraction history of the Moon.

The radial expansion/contraction history depends on the spatial dimensionality. In a spherically symmetric model where the distribution of melt-content depends only on the radial coordinate r, the amplitude of radial expansion is around 1.2 km (see Figure 2 in U et al. (2022)). In contrast, the amplitude in our 2-D model is around 3 km (Figure 4), substantially larger than that in the 1-D model. To predict more quantitatively the radial expansion/contraction history of the Moon, it is necessary to develop a model in a 3-D spherical shell (Laneuville et al., 2013; N. Zhang et al., 2013a, 2013b).

4.2. Comparison With the Observed Features of the Moon

4.2.1. The Radial Expansion/Contraction

The Moon globally expands by a few kilometers for the first several hundred million years in our reference case owing to the volume change caused by melting of the mantle (Figure 4). The timing and amplitude of radial expansion are consistent with those of the Moon inferred from its gravity field in the literature (Andrews-Hanna et al., 2013, 2014; Liang & Andrews-Hanna, 2022; Sawada et al., 2016). After the radial expansion, the Moon begins to radially contract at around 1 Gyr after the start of the calculation (Figure 4). The timing of contraction is consistent with the beginning of compressive tectonics on the Moon (Frueh et al., 2023; Yue et al., 2017). The Moon in our model contracts at a rate of approximately -1.0 km Gyr^{-1} in the past billion years (Table 3), which is also consistent with the estimates obtained from observations of fault scarps on the Moon (e.g., Clark et al., 2017; Klimczak, 2015; van der Bogert et al., 2018; Watters et al., 2010). As a whole, the calculated history of radius change of the reference case is consistent with that of the Moon.

Among our models presented in Figure 14, the radius changes calculated at $M^* \geq 50$, $T_p \approx 1600$ K, and $F_{crst}{}^* \leq 16$ are consistent with the observed one. When the reference permeability M^* is lower than 50, the amplitude of radial expansion is much larger than the estimate for the Moon because generated magma in the deep mantle stays there for a long time (Figures 6 and 14a). In the cases where the initial concentration ratio of the HPEs in the crust to the mantle $F_{crst}{}^*$ is larger than 16 (the average heating rate in the mantle is less than 7.6 pW kg^{-1} in the initial condition), sufficient partially molten regions cannot develop to cause the early expansion (Figure 14b). Our models also show that the timing and amplitude of radial expansion strongly depend on the presence of overturned IBC components enriched layer l^* (Figure 14d and Table 3). In Case l0 where the overturned layer is not assumed ($1/l^* = 0$), indeed, the timing and amplitude of calculated radial expansion are later and smaller than the observed expansion.

Our models suggest that a substantial fraction of the mantle should have been solid at the beginning of the lunar history for the observed early expansion to take place (Figures 1a and 14c). This result urges us to rethink the lunar formation process. Many of previous simulations of the lunar formation suggest that most materials were hot enough to evaporate immediately after the Moon-forming giant impact (e.g., Canup, 2014; Lock et al., 2018). A substantial fraction of the mantle may have been still molten at the beginning of the lunar evolutionary history after the mantle overturn if the Moon was formed so hot. The more solid mantle after the mantle overturn we suggest here would be more consistent with the "immediate origin" model of the Moon (Kegerreis et al., 2022) where the giant impact is simulated at a resolution more than one order of magnitude higher than that employed in earlier studies; this model suggests that the outer material of the Moon is heated to at least 4000 K by the impact, but the deeper interior is only a few hundred Kelvin warmer than the pre-impact temperature, assumed to be around 2000 K. (Note that our preferred initial potential temperature of around 1600 K (Figure 14c) is consistent with the temperature after the mantle overturn in the earlier models of H. Li et al. (2019) and Yu et al. (2019) where the temperature of the pre-overturn mantle is assumed to be around 2000 K close to the value suggested by Kegerreis et al. (2022)).

4.2.2. The Volcanic Activity

Our reference case is also consistent with the observed history of mare volcanism of the Moon. For the first 0.4 Gyr of the calculated history, the partially molten regions in the deep mantle grow only slowly, while the partially molten region in the uppermost mantle shrinks over time (Figure 2). This early stage is likely to correspond to the period during which mare volcanism on the Moon was not so active (e.g., Hiesinger et al., 2003; Whitten & Head, 2015). The growth of melt-fingers and subsequent partially molten plumes observed in Figure 2b account for the lunar mare volcanism that became active after around 4 Gyr ago and peaked at 3.5–3.8 Gyr ago, and then gradually declined over a period of billions of years (e.g., Hiesinger et al., 2000; Morota et al., 2011); the calculated activity of partially molten plumes is indeed peaked at around 3.7 Gyr ago and then gradually declines with time. These overall features of the calculated volcanic history are not affected by the detail of the rheology (Section 3.3) and possible density inversion between melts and matrix (Section 3.4). In contrast, in a model where plumes do not appear (Case Ra2.15e4 calculated at lower Rayleigh number $\mathrm{Ra} = 2.15 \times 10^4$), the volcanic activity develops only during the first several million years by melt-fingers (Figure 6b), suggesting that partially molten plumes play an important role in the volcanic history of the Moon.

Note that magma not enriched in HPEs is generated in the latter period of the calculated history (Figure 2 for 1.44 Gyr). This volcanism is caused by a return flow of a foundering material enriched in IBC components (see

the arrow in Figure 2d). This may account for the volcanism of HPE-depleted young basalts (Che et al., 2021; Q.-L. Li et al., 2021; Su et al., 2022).

4.2.3. The Temperature Profile

The depth-profile of the horizontally averaged temperature calculated at 4.4 Gyr in our reference case shows that the lithosphere develops as a thermal boundary layer of the convective mantle (Figure 3a), while the temperature profile suggested for the present Moon (e.g., Karato, 2013; Khan et al., 2006, 2014; Sonett, 1982) is closer to a thermal diffusion profile. The difference is not large in the shallow mantle (until the depth level of around 200 km), but the calculated temperature in the mid-mantle is considerably higher than that in the present Moon (Figure 3a). As a consequence, the mantle is partially molten in the mid-mantle (from around r = 1,100–1,300 km), whereas seismic evidence suggests that the partially molten region occurs only at the base of the mantle (e.g., Latham et al., 1973; Nakamura et al., 1973; Tan & Harada, 2021; Weber et al., 2011). A temperature profile consistent with the observed one was not obtained at other parameter values (Figure 3a). This difficulty may be a consequence of the assumed 2-D polar rectangular geometry of the convecting vessel and calls for further numerical calculations in a 3-D spherical shell where the mid-mantle tends to be more strongly cooled and mantle convection is more sluggish (Guerrero et al., 2018).

5. Conclusions

To understand the volcanic and radial expansion/contraction history of the Moon, we developed a 2-D polar rectangular numerical model of mantle evolution illustrated in Figure 15. The internally heated mantle of the model evolves by the transport of heat, mass, and HPEs by mantle convection and migrating magma that is generated by decompression melting and internal heating.

Our simulations show that magma generation and migration play a crucial role in the volcanic and radial expansion/contraction history of the Moon. Magma is generated in the deep mantle by internal heating and eventually ascends to the surface as partially molten plumes driven by melt buoyancy for the first several hundred million years (Figures 2 and 15). This stage is likely to correspond to the period during which mare volcanism became active after 4 Gyr ago with the peak at 3.5–3.8 Gyr ago (e.g., Whitten & Head, 2015). Subsequent magma ascents by partially molten plumes decline with time but continue for billions of years after the peak because some materials that host HPEs are enriched in the IBC and remain in the deep mantle by their negative buoyancy (Figure 2). This activity accounts for the lunar mare volcanism that gradually declined after the peak (e.g., Hiesinger et al., 2003). The model which accounts for the observed mare volcanism is also consistent with the radial expansion/contraction history of the Moon, which globally expanded in its earlier history until around 3.8 Gyr ago and then contracted with time (e.g., Andrews-Hanna et al., 2013; Frueh et al., 2023). In our model, the Moon expands by a few kilometers for the first several hundred million years and then contracts over time (Figure 4). The lunar expansion is due to the extension of partially molten regions by partially molten plumes that extract magma generated in the deep mantle (Figures 6a and 14); the subsequent contraction is caused by solidification of the regions due to cooling from the surface boundary. The early expansion by mantle melting suggested here implies that a substantial fraction of the mantle should have been solid, and there was a layer enriched in HPEs and the IBC components at the base of the mantle in the Moon at the beginning of its history (Figures 13, 14c, and 14d and Table 3). In order to construct a more realistic thermal history model of the Moon, it is necessary to extend our model to a 3-D spherical shell geometry and to introduce a lateral heterogeneity in the initial thermal and compositional condition in future work.

Appendix A: The Basic Equations

In this section, we describe the basic equations that are not referred in Section 2.1. The continuity equation is

$$\nabla \cdot \mathbf{U} = -\nabla \cdot [\phi(\mathbf{u} - \mathbf{U})]. \tag{A1}$$

The momentum equation for mantle convection is

$$-\nabla P + \rho g + \nabla \cdot \left[\eta\left(\nabla \mathbf{U} + {}^{t}\nabla \mathbf{U}\right)\right] = 0. \tag{A2}$$

Where the superscript t means transpose of a matrix.

Migration of magma is calculated in the energy equation (Katz, 2008),

$$\frac{\partial(\rho_0 h)}{\partial t} + \nabla\cdot(\rho_0 h\mathbf{U}) = -\nabla\cdot[\rho_0 h_l\phi(\mathbf{u}-\mathbf{U})] - \frac{\Delta v_l}{v_0}\rho_0 g\phi u_r + \nabla\cdot(k\nabla T) + \rho_0 q + \nabla\cdot[\kappa_{\mathrm{edd}}\nabla(\rho_0 h)], \tag{A3}$$

where $h_l = h(\phi = 1)$. $k = \rho_0 C_p \kappa$ is the thermal conductivity, and κ is the thermal diffusivity. We assumed that the matrix disintegrates and that a strong turbulent diffusion occurs with the eddy diffusivity of $\kappa_{\mathrm{edd}} = 50\kappa$ in a largely molten region with $\phi > 0.4$ (Kameyama et al., 1996; Ogawa, 2020). κ_{edd} is assumed to gradually increase with increasing ϕ as ϕ^3 (Ogawa, 2018b; U et al., 2022). We also assumed that the crustal thermal diffusivity is 0.48 times smaller than the mantle thermal diffusivity, taking into account the blanket effect of the crust and regolith layers (Ziethe et al., 2009).

We calculate the phase diagram of the binary eutectic materials $A_\xi B_{1-\xi}$ as well as the temperature, and melt-content from the chemical potential defined for the materials. In the solid phase, the chemical potential μ^{solid} is

$$\mu^{solid} = -C_p T/\sigma_A - T(S_0 + C_p \ln T/\sigma_A) + P/\rho_0 \tag{A4}$$

for both of the end-members A and B where S_0 is an arbitrary constant. In the liquid state where the melt behaves ideal solution in this model, the chemical potential μ^{liquid} of the end-members i ($i = A, B$) is

$$\mu_i^{liquid} = \mu_i^{l0} + RT\ln\xi_i^{liquid}, \tag{A5}$$

and

$$\mu_i^{l0} = \mu^{solid} + \Delta h/\sigma_i\left(1 + G - T/T_i^{l0}\right). \tag{A6}$$

Here, R is the gas constant 8.3 J mol^{-1} K^{-1}; σ_i the molar mass of each end-members (A = 140.69 g mol^{-1}; B = 151.71 g mol^{-1}); T_i^{l0} the dry solidus of the end member i at zero-pressure.

The core is regarded as a heat bath of a uniform temperature T_c that changes with time as

$$c_{pc}\rho_{\mathrm{core}}V_{\mathrm{core}}\frac{dT_c}{dt} = -Sf, \tag{A7}$$

where c_{pc} = 675 J K^{-1} kg^{-1} (Ziethe et al., 2009) is the specific heat of the core, ρ_{core} = 6,200 kg m^{-3} (Kronrod et al., 2022) the core density, V_{core} the volume of the core, and S the surface area of the CMB. The heat flux at the CMB f is calculated from

$$f = -\frac{1}{\pi}\int_0^\pi \left(k\frac{\partial T}{\partial r}\right)_{r=r_c} d\theta. \tag{A8}$$

In this study, we neglect the internal heating in the core.

The heating rate q changes with time as

$$q = q_{\mathrm{tr}}^* q_0 \exp\left(-\frac{t}{\tau}\right), \tag{A9}$$

where q_0 = 14.7 pW kg^{-1} is the average initial heating rate at 4.4 Gyr ago estimated from the total amount of HPEs in the current Moon (see Table 2 in U et al. (2022)); τ the decay time of HPEs. We approximate this value as τ = 1.5 Gyr, an average of the decay times of ^{235}U and ^{40}K (Kameyama et al., 1996; Ogawa, 2020). The non-dimensional value q_{tr}^* changes with migrating magma as

$$\frac{\partial q_{\mathrm{tr}}^*}{\partial t} + \nabla\cdot\left(q_{\mathrm{tr}}^*\mathbf{U}\right) = -\nabla\cdot\left[q_l^*\phi(\mathbf{u}-\mathbf{U})\right] + \nabla\cdot\left(\kappa_{\mathrm{edd}}\nabla q_{\mathrm{tr}}^*\right). \tag{A10}$$

Here, q_l^* is the internal heating rate in the melt as

$$q_l^* = \frac{Dq_{\mathrm{tr}}^*}{(D-1)\phi + 1}, \tag{A11}$$

and, $D = 100$ is the partition coefficient of HPEs between the solid phase and the melt phase.

The bulk composition ξ_b also changes with time owing to the mass transport by melt and matrix as

$$\frac{\partial \xi_b}{\partial t} + \nabla \cdot (\xi_b \mathbf{U}) = -\nabla \cdot [\xi_l \phi(\mathbf{u} - \mathbf{U})] + \nabla \cdot [\kappa_{edd} \nabla(\xi_b)]. \tag{A12}$$

The basic equations are converted into their non-dimensional forms using the length scale $L = r_p - r_c$, the temperature scale $\Delta h/C_p$, and times scale L^2/κ. The momentum equation in its non-dimensional form is

$$-\nabla P^* + Ra\rho^* \mathbf{e_r} + \nabla \cdot \left[\eta^* \left(\nabla \mathbf{U}^* + {}^t\nabla \mathbf{U}^*\right)\right] = 0. \tag{A13}$$

where

$$\eta^* = \exp\left[E_T^* \left(T_{ref}^* - T^*\right)\right]. \tag{A14}$$

The non-dimensional relative velocity $\mathbf{u}^* - \mathbf{U}^*$ is written as

$$\mathbf{u}^* - \mathbf{U}^* = -M^* g^* \frac{\phi^2}{\phi_0^3} \left\{ \frac{\Delta v_l}{v_0} [1 + \beta(1 - \xi_l)] - \beta(\xi_s - \xi_l) \right\} \mathbf{e_r}. \tag{A15}$$

The non-dimensional energy equation is written as

$$\begin{aligned} \frac{\partial h^*}{\partial t} + \nabla \cdot (h^* \mathbf{U}^*) = &- \nabla \cdot \left[h_l^* \phi(\mathbf{u}^* - \mathbf{U}^*)\right] - N^* g^* \frac{\Delta v_l}{v_0} \phi u_r^* + \nabla \cdot (\kappa^* \nabla T^*) \\ &+ q^* + \nabla \cdot \left(\kappa_{edd}^* \nabla h^*\right), \end{aligned} \tag{A16}$$

where $h^* = T^* + \phi(1 + G)$, and $N^* \equiv g_{sur} L/\Delta h$.

Appendix B: Details of the Initial Condition

In this section, we describe the details of the initial condition. The initial distribution of the temperature is obtained from that of the "reduced" enthalpy (see Equation 4), which is

$$h = \min(h_{sur}, h_{mantle}), \tag{B1}$$

where

$$h_{sur} = C_p \left[T_{sur} + \delta_{crst} \left(1 - \frac{r}{r_p}\right)\right], \tag{B2}$$

$$h_{mantle} = \begin{cases} C_p T_p & \text{if } r > r_l \\ C_p \left[T_p + \left(T_c - T_p\right) \left(\frac{r_l - r}{r_l - r_c}\right)^2\right] & \text{if } r < r_l \end{cases}. \tag{B3}$$

Here, δ_{crst} and r_l are constants arbitrarily chosen. We assumed $\delta_{crst} = 79.5 \times 10^3$ K to mimic the temperature-increase with depth in the topmost 35 km (i.e., the crust) of the Moon, and $r_l = 550$ km which is estimated from earlier numerical models of the post-overturn stratification (e.g., Boukaré et al., 2018; Mitchell, 2021). T_p is the potential temperature; $T_c = 1875$ K the initial temperature of the core. The value of T_c is based on the assumption that the temperature of the core is higher than the mantle at 4.4 Gyr ago (Alley & Parmentier, 1998; Boukaré et al., 2018; Maurice et al., 2020; Morbidelli et al., 2018). (Note that r_l is not well-constrained from earlier modeling studies. To see how r_l affects our numerical results, we calculated Case rl-100 km where r_l is 100 km and described this case in Text S3 of the Supporting Information S1. As discussed there, we confirmed that the reduction in r_l does not influence the overall features of mantle evolution observed in the reference case although found that the Moon contracts by −2 km for the first 100 Myr. The early contraction is caused by a rapid cooling of the core (see Equation 12), which occurs because the reduction in r_l enhances the heat flow at the CMB.)

We assumed that the initial distribution of internal heat source q satisfies $\int_{r_c}^{r_p} qr dr = \int_{r_c}^{r_p} q_0 r dr$, where $q_0 = 14.7$ pW kg^{-1} is the average value of internal heating rate at 4.4 Gyr ago (Laneuville et al., 2018; U

et al., 2022). The total initial heating rate in the topmost 35 km q_{crst} is F^*_{crst} times higher than that in the mantle (see Table 2):

$$F^*_{crst} = \frac{\int_{r_{crst}}^{r_p} q_{crst} r dr}{\int_{r_c}^{r_{crst}} q_m r dr}, \tag{B4}$$

where,

$$\int_{r_c}^{r_{crst}} q_m r dr = \int_{r_c}^{r_p} q_0 r dr - \int_{r_{crst}}^{r_p} q_{crst} r dr. \tag{B5}$$

We assumed the initial distribution of internal heating rate in the mantle q_m to be

$$q_m = q_{ol} + q_{add}, \tag{B6}$$

where $q_{ol} = 2.77$ pW kg^{-1} is the internal heating rate of the olivine-rich materials with $\xi_b = 1$ (Yu et al., 2019), while q_{add} is that of additional IBC components that increases with depth as

$$q_{add} = \Delta q \exp\left[-\frac{r - r_c}{l}\right]. \tag{B7}$$

Here, l is the thickness of the basal layer which is enriched in the overturned materials (see Table 2); Δq is a constant which is calculated from

$$\int_{r_c}^{r_{crst}} q_m r dr = \int_{r_c}^{r_{crst}} q_{ol} r dr + \int_{r_c}^{r_{crst}} q_{add} r dr. \tag{B8}$$

We calculated the initial distribution of the bulk composition ξ_b in the mantle from that of the internal heating rate. We assumed that the IBC components with the composition $\xi_e = 0.1$ are 7.5 times more enriched in HPEs than the bulk silicate Moon q_0 (Hess & Parmentier, 1995) and that the initial content of the IBC components is proportional to q_{add} as

$$\frac{1 - \xi_b}{1 - \xi_e} = \frac{q_{add}}{7.5 q_0}. \tag{B9}$$

In the topmost 35 km, where we assumed $\xi_b = 1$ for simplicity.

Acknowledgments
The authors would like to extend their sincere appreciation to T. Yanagisawa and T. Miyagoshi at JAMSTEC for their constructive comments. The authors also thank the editor L. Montési, and the anonymous reviewers for their insightful comments and suggestions, which helped improve the quality of this paper. This work was supported by JST SPRING, Grant JP-MJSP2108 of Japan. This work was also supported by: the Joint Usage/Research Center PRIUS at Ehime University, the Earth Simulator of Japan Agency for Marine-Earth Science and Technology (JAMSTEC), "Exploratory Challenge on Post-K Computer" (Elucidation of the Birth of Exoplanets [Second Earth] and the Environmental Variations of Planets in the Solar System), and "Program for Promoting Research on the Supercomputer Fugaku" (Toward a unified view of the universe: from large scale structures to planets). Animations and some figures were drawn with the ParaView by Sandia National Laboratory, Kitware Inc., and Los Alamos National Laboratory.

Data Availability Statement

The original data used to produce Table 3 and figures, the plots of Figures 1, 3, 4, and 14 as well as the numerical code used to construct this work are found at U et al. (2023).

References

Alley, K. M., & Parmentier, E. M. (1998). Numerical experiments on thermal convection in a chemically stratified viscous fluid heated from below: Implications for a model of lunar evolution. *Physics of the Earth and Planetary Interiors*, *108*(1), 15–32. https://doi.org/10.1016/S0031-9201(98)00096-X

Andrews-Hanna, J. C., Asmar, S. W., Head, J. W., III, Kiefer, W. S., Konopliv, A. S., Lemoine, F. G., et al. (2013). Ancient igneous intrusions and early expansion of the Moon revealed by GRAIL gravity gradiometry. *Science*, *339*(6120), 675–678. https://doi.org/10.1126/science.1231753

Andrews-Hanna, J. C., Besserer, J., Head, J. W., III., Howett, C. J. A., Kiefer, W. S., Lucey, P. J., et al. (2014). Structure and evolution of the lunar procellarum region as revealed by grail gravity data. *Nature*, *514*(7520), 68–71. https://doi.org/10.1038/nature13697

Arai, T., Terada, H., Yamaguchi, A., & Ohtake, M. (2008). A new model of lunar crust: Asymmetry in crustal composition and evolution. *Earth Planets and Space*, *60*(4), 433–444. https://doi.org/10.1186/BF03352808

Boukaré, C.-E., Parmentier, E. M., & Parman, S. W. (2018). Timing of mantle overturn during magma ocean solidification. *Earth and Planetary Science Letters*, *491*(1), 216–225. https://doi.org/10.1016/j.epsl.2018.03.037

Breuer, D., & Moore, W. (2015). 10.08—Dynamics and thermal history of the terrestrial planets, the Moon, and Io. In G. Schubert (Ed.), *Treatise on geophysics* (2nd ed., pp. 255–305). https://doi.org/10.1016/B978-0-444-53802-4.00173-1

Canup, R. M. (2004). Simulations of a late lunar-forming impact. *Icarus*, *168*(2), 433–456. https://doi.org/10.1016/j.icarus.2003.09.028

Canup, R. M. (2014). Lunar-forming impacts: Processes and alternatives. *Philosophical Transactions of the Royal Society A: Mathematical, Physical and Engineering Sciences*, *372*(2024), 20130175. https://doi.org/10.1098/rsta.2013.0175

Cassen, R., & Reynolds, R. T. (1973). Role of convection in the Moon. *Journal of Geophysical Research*, *78*(17), 3203–3215. https://doi.org/10.1029/JB078i017p03203

Cassen, R., Reynolds, R. T., Graziani, F., Summers, A., McNellis, J., & Blalock, L. (1979). Convection and lunar thermal history. *Physics of the Earth and Planetary Interiors*, *19*(2), 183–196. https://doi.org/10.1016/0031-9201(79)90082-7

Che, X., Nemchin, A., Liu, T., Long, D., Norman, M. D., Joy, K. H., et al. (2021). Age and composition of young basalts on the Moon, measured from samples returned by Chang'e-5. *Science*, *374*(6569), 887–890. https://doi.org/10.1126/science.abl7957

Cho, Y., Morota, T., Haruyama, J., Yasui, M., Hirata, N., & Sugita, S. (2012). Young mare volcanism in the Orientale region contemporary with the Procellarum KREEP terrane (PKT) volcanism peak period around 2 billion years ago. *Geophysical Research Letters*, *39*(11), L11203. https://doi.org/10.1029/2012GL051838

Clark, J. M., Hurtado, J. D., Jr., Hiesinger, H., van der Bogert, C. H., & Bernhardt, H. (2017). Investigation of newly discovered lobate scarps: Implications for the tectonic and thermal evolution of the Moon. *Icarus*, *298*, 78–88. https://doi.org/10.1016/j.icarus.2017.08.017

Cuk, M., & Stewart, S. T. (2012). Making the Moon from a fast-spinning Earth: A giant impact followed by resonant despinning. *Science*, *338*(1047), 1047–1052. https://doi.org/10.1126/science.1225542

de Vries, J., van den Berg, A., & van Westrenen, W. (2010). Formation and evolution of a lunar core from ilmenite-rich magma ocean cumulates. *Earth and Planetary Science Letters*, *292*(1–2), 139–147. https://doi.org/10.1016/j.epsl.2010.01.029

Dumoulin, C., Doin, M.-P., & Fleitout, L. (1999). Heat transport in stagnant lid convection with temperature- and pressure-dependent Newtonian or non-Newtonian rheology. *Journal of Geophysical Research*, *104*(B6), 12759–12777. https://doi.org/10.1029/1999JB900110

Dygert, N., Hirth, G., & Liang, Y. (2016). A flow law for ilmenite in dislocation creep: Implications for lunar cumulate mantle overturn. *Geophysical Research Letters*, *43*(2), 532–540. https://doi.org/10.1002/2015GL066546

Elkins-Tanton, L., & Bercovici, D. (2014). Contraction or expansion of the Moon's crust during magma ocean freezing? *Philosophical Transactions of the Royal Society A: Mathematical, Physical and Engineering Sciences*, *372*(2024), 20130240. https://doi.org/10.1098/rsta.2013.0240

Elkins-Tanton, L., Burgess, S., & Yin, Q.-Z. (2011). The lunar magma ocean: Reconciling the solidification process with lunar petrology and geochronology. *Earth and Planetary Science Letters*, *304*(3–4), 326–336. https://doi.org/10.1016/j.epsl.2011.02.004

Frueh, T., Hiesinger, H., Bogert, C. H., Clark, J. D., Watters, T. R., & Schmedemann, N. (2023). Timing and origin of compressional tectonism in mare tranquillitatis. *Journal of Geophysical Research: Planets*, *128*, e2022JE007533. https://doi.org/10.1029/2022JE0075

Garcia, R. F., Gagnepain-Beyneix, J., Chevrot, S., & Lognonné, P. (2011). Very preliminary reference Moon model. *Journal of Geophysical Research*, *188*(1–2), 96–113. https://doi.org/10.1016/j.pepi.2011.06.015

Garcia, R. F., Gagnepain-Beyneix, J., Chevrot, S., & Lognonné, P. (2012). Erratum to "very preliminary reference Moon model". *Physics of the Earth and Planetary Interiors*, *202–203*, 89–91. https://doi.org/10.1016/j.pepi.2012.03.009

Guerrero, J. M., Lowman, J. P., Deschamps, F., & Tackley, P. J. (2018). The influence of curvature on convection in a temperature-dependent viscosity fluid: Implications for the 2-D and 3-D modeling of Moon's. *Journal of Geophysical Research: Planets*, *123*(7), 1863–1880. https://doi.org/10.1029/2017JE005497

Head, J. W., & Wilson, L. (1992). Lunar mare volcanism: Stratigraphy, eruption conditions, and the evolution of secondary crusts. *Geochimica et Cosmochimica Acta*, *56*(6), 2155–2175. https://doi.org/10.1016/0016-7037(92)90183-J

Head, J. W., & Wilson, L. (2017). Generation, ascent and eruption of magma on the Moon: New insights into source depths, magma supply, intrusions and effusive/explosive eruptions (part 2: Predicted emplacement processes and observations). *Icarus*, *283*, 176–223. https://doi.org/10.1016/j.icarus.2016.05.031

Head, J. W., & Wilson, L. (2020). Magmatic intrusion-related processes in the upper lunar crust: The role of country rock porosity/permeability in magmatic percolation and thermal annealing, and implications for gravity signatures. *Planetary and Space Science*, *180*, 104765. https://doi.org/10.1016/j.pss.2019.104765

Hess, P. C., & Parmentier, E. M. (1995). A model for the thermal and chemical evolution of the Moon's interior: Implications for the onset of mare volcanism. *Earth and Planetary Science Letters*, *134*(3–4), 501–514. https://doi.org/10.1016/0012-821X(95)00138-3

Hess, P. C., & Parmentier, E. M. (2001). Thermal evolution of a thicker KREEP liquid layer. *Journal of Geophysical Research*, *106*(E11), 28023–28032. https://doi.org/10.1029/2000JE001416

Hiesinger, H., Head, J. W., III., Wolf, U., Jaumann, R., & Neukum, G. (2003). Ages and stratigraphy of mare basalts in Oceanus Procellarum, Mare Nubium, Mare Cognitum, and Mare Insularum. *Journal of Geophysical Research*, *108*(E7), 5065. https://doi.org/10.1029/2002JE001985

Hiesinger, H., Jaumann, R., Neukum, G., & Head, J. W. (2000). Ages and stratigraphy of mare basalts in Oceanus Procellarum, Mare Nubium, Mare Cognitum, and Mare Insularum. *Journal of Geophysical Research*, *105*(E12), 29239–29275. https://doi.org/10.1029/2000JE001244

Hirth, G., & Kohlstedt, D. L. (2003). Rheology of the upper mantle and the mantle wedge: A view from the experimentalists. *Geophysical Monograph Series*, *138*, 83–105. https://doi.org/10.1029/138GM06

Hosono, N., Karato, S.-I., Makino, J., & Saitoh, T. R. (2019). Terrestrial magma ocean origin of the Moon. *Nature Geoscience*, *12*(6), 418–423. https://doi.org/10.1038/s41561-019-0354-2

Jolliff, B. L., Gillis, J. J., Haskin, L., Korotev, R. L., & Wieczorek, M. A. (2000). Major lunar crustal terranes: Surface expressions and crustal-mantle origins. *Journal of Geophysical Research*, *105*(E2), 4197–4216. https://doi.org/10.1029/1999JE001103

Jones, M. J., Evans, A. J., Johnson, B. C., Weller, M. B., Andrews-Hanna, J. C., Tikoo, S. M., & Keane, J. T. (2022). A South Pole–Aitken impact origin of the lunar compositional asymmetry. *Science Advances*, *8*(14). https://doi.org/10.1126/sciadv.abm8475

Kameyama, M., Fujimoto, H., & Ogawa, M. (1996). A thermo-chemical regime in the upper mantle in the early Earth inferred from a numerical model of magma-migration in a convecting upper mantle. *Physics of the Earth and Planetary Interiors*, *94*(3–4), 187–215. https://doi.org/10.1016/0031-9201(95)03102-2

Karato, S. (2013). Geophysical constraints on the water content of the lunar mantle and its implications for the origin of the Moon. *Earth and Planetary Science Letters*, *384*, 144–153. https://doi.org/10.1016/j.epsl.2013.10.001

Karato, S., & Wu, P. (1993). Rheology of the upper mantle: A synthesis. *Science*, *260*(5109), 771–778. https://doi.org/10.1126/science.260.5109.771

Katz, R. F. (2008). Magma dynamics with the enthalpy method: Benchmark solutions and magmatic focusing at mid-ocean ridges. *Geochemistry, Geophysics, Geosystems*, *49*(12), 2099–2121. https://doi.org/10.1093/petrology/egn058

Katz, R. F., Spiegelman, M., & Langmuir, C. H. (2003). A new parameterization of hydrous mantle melting. *Geochemistry, Geophysics, Geosystems*, *4*(9), 1073. https://doi.org/10.1029/2002GC000433

Kegerreis, J. A., Ruiz-Bonilla, S., Eke, V. R., Massey, R. J., Sandnes, T. D., & Teodoro, L. F. A. (2022). Immediate origin of the Moon as a post-impact satellite. *The Astrophysical Journal Letters*, *937*(2), L40. https://doi.org/10.3847/2041-8213/ac8d96

Khan, A., Connolly, J. A. D., Pommier, A., & Noir, J. (2014). Geophysical evidence for melt in the deep lunar interior and implications for lunar evolution. *Journal of Geophysical Research: Planets*, *119*(10), 2197–2221. https://doi.org/10.1002/2014JE004661

Khan, A., Maclennan, J., Taylor, S. R., & Connolly, J. A. D. (2006). Are the Earth and the Moon compositionally alike? Inferences on lunar composition and implications for lunar origin and evolution from geophysical modeling. *Journal of Geophysical Research*, *111*(E5), E05005. https://doi.org/10.1029/2005JE002608

Kirk, R. L., & Stevenson, D. J. (1989). The competition between thermal contraction and differentiation in the stress history of the Moon. *Journal of Geophysical Research*, *94*(B9), 12133–12144. https://doi.org/10.1029/JB094iB09p12133
Klimczak, C. (2015). Limits on the brittle strength of planetary lithospheres undergoing global contraction. *Journal of Geophysical Research: Planets*, *120*(12), 2135–2151. https://doi.org/10.1002/2015JE004851
Konrad, W., & Spohn, T. (1997). Thermal history of the Moon: Implications for an early core dynamo and post-accretional magmatism. *Advances in Space Research*, *19*(10), 1511–1521. https://doi.org/10.1016/S0273-1177(97)00364-5
Kronrod, E., Matsumoto, K., Kuskov, O. L., Kronrod, V., Yamada, R., & Kamata, S. (2022). Towards geochemical alternatives to geophysical models of the internal structure of the lunar mantle and core. *Advances in Space Research*, *69*(7), 2798–2824. https://doi.org/10.1016/j.asr.2022.01.012
Laneuville, M., Taylor, J., & Wieczorek, M. A. (2018). Distribution of radioactive heat sources and thermal history of the Moon. *Journal of Geophysical Research: Planets*, *123*(12), 3144–3166. https://doi.org/10.1029/2018JE005742
Laneuville, M., Wieczorek, M. A., Breuer, D., Aubert, J., & Ruckriemen, T. (2014). A long-lived lunar dynamo powered by core crystallization. *Earth and Planetary Science Letters*, *401*, 251–260. https://doi.org/10.1016/j.epsl.2014.05.057
Laneuville, M., Wieczorek, M. A., Breuer, D., & Tosi, N. (2013). Asymmetric thermal evolution of the Moon. *Journal of Geophysical Research: Planets*, *118*(7), 1435–1452. https://doi.org/10.1002/jgre.20103
Latham, G., Dorman, J., Duennebier, F., Ewing, M., Lammlein, D., & Nakamura, Y. (1973). Moonquakes, meteoroids, and the state of the lunar interior. In *Proceedings of the lunar science conference* (Vol. 4, pp. 2515–2527).
Lawrence, D. J., Feldman, W. C., Barraclough, B. L., Binder, A. B., Elphic, R. C., Maurice, S., et al. (2000). Small-area thorium features on the lunar surface. *Journal of Geophysical Research*, *105*(E8), 20307–20331. https://doi.org/10.1029/1999JE001177
Le Bars, M., & Davaille, A. (2004). Whole layer convection in a heterogeneous planetary mantle. *Journal of Geophysical Research*, *109*(B3), B03403. https://doi.org/10.1029/2003JB002617
Li, H., Zhang, N., Ling, Y., Wu, B., Dygert, N. K., Huang, J., & Parmentier, E. M. (2019). Lunar cumulate mantle overturn: A model constrained by ilmenite rheology. *Journal of Geophysical Research: Planets*, *124*(5), 1357–1378. https://doi.org/10.1029/2018JE005905
Li, Q.-L., Zhou, Q., Liu, Y., Xiao, Z., Lin, Y., Li, J.-H., et al. (2021). Two-billion-year-old volcanism on the Moon from Chang'e-5 basalts. *Nature*, *600*(7887), 54–58. https://doi.org/10.1038/s41586-021-04100-2
Liang, W., & Andrews-Hanna, J. C. (2022). Probing the source of ancient linear gravity anomalies on the Moon. *Icarus*, *380*, 114978. https://doi.org/10.1016/j.icarus.2022.114978
Lock, S., Stewart, S., Petaev, M., Leinhardt, z., Mace, M., Jacobsen, S., & Cuk, M. (2018). The origin of the Moon within a terrestrial synestia. *Journal of Geophysical Research: Planets*, *123*(4), 910–951. https://doi.org/10.1002/2017JE005333
Lourenço, D. L., Rozel, A. B., Gerya, T., & Tackley, P. J. (2018). Efficient cooling of rocky planets by intrusive magmatism. *Journal of Geophysical Research*, *11*(5), 322–327. https://doi.org/10.1038/s41561-018-0094-8
Matsuyama, L., Keane, J. T., Trinh, A., Beuthe, M., & Watters, T. R. (2021). Global tectonic patterns of the Moon. *Geophysical Research Letters*, *358*(114202), 114202. https://doi.org/10.1016/j.icarus.2020.114202
Maurice, M., Tosi, N., Schwinger, S., Breuer, D., & Kleine, T. (2020). A long-lived magma ocean on a young Moon. *Science Advances*, *6*(28). https://doi.org/10.1126/sciadv.aba8949
McKenzie, D. (1984). The generation and compaction of partially molten rock. *Journal of Petrology*, *25*(3), 713–765. https://doi.org/10.1093/petrology/25.3.713
Mei, S., Bai, W., Hiraga, T., & Kohlstedt, D. L. (2002). Influence of melt on the creep behavior of olivine–basalt aggregates under hydrous conditions. *Earth and Planetary Science Letters*, *201*(3–4), 491–507. https://doi.org/10.1016/S0012-821X(02)00745-8
Miller, K. J., Zhu, W.-L., Montési, L. G. J., & Gaetani, G. A. (2014). Experimental quantification of permeability of partially molten mantle rock. *Earth and Planetary Science Letters*, *388*(15), 273–282. https://doi.org/10.1016/j.epsl.2013.12.003
Mitchell, R. N. (2021). Chang'e-5 reveals the Moon's secrets to a longer life. *The Innovation*, *2*(4), 100177. https://doi.org/10.1016/j.xinn.2021.100177
Morbidelli, A., Nesvorny, D., Laurenz, V., Marchi, S., Rubie, D. C., Elkins-Tanton, L., et al. (2018). The timeline of the lunar bombardment: Revisited. *Icarus*, *305*, 262–276. https://doi.org/10.1016/j.icarus.2017.12.046
Moriarty, D. P., III., Dygert, N., Valencia, S. N., Watkins, R. N., & Petro, N. E. (2021). The search for lunar mantle rocks exposed on the surface of the Moon. *Nature Communications*, *12*(4659), 4659. https://doi.org/10.1038/s41467-021-24626-3
Morota, T., Haruyama, J., Honda, C., Ohtake, M., Yokota, Y., Kimura, J., et al. (2009). Mare volcanism in the lunar farside Moscoviense region: Implication for lateral variation in magma production of the Moon. *Geophysical Research Letters*, *36*(21), L21202. https://doi.org/10.1029/2009GL040472
Morota, T., Haruyama, J., Ohtake, M., Matsunaga, T., Kawamura, T., Yokota, Y., et al. (2011). Timing and duration of mare volcanism in the central region of the northern farside of the Moon. *Earth Planets and Space*, *63*(1), 5–11. https://doi.org/10.5047/eps.2010.02.009
Nakamura, Y., Lammlein, D., Latham, G., Ewing, M., Dorman, J., Press, F., & Toksöz, N. (1973). New seismic data on the state of the deep lunar interior. *Science*, *181*(4094), 49–51. https://doi.org/10.1126/science.181.4094.49
Newsom, H. E., & Taylor, S. R. (1989). Geochemical implications of the formation of the Moon by a single giant impact. *Nature*, *338*(6210), 29–34. https://doi.org/10.1038/338029a0
Ogawa, M. (2014). A positive feedback between magmatism and mantle upwelling in terrestrial planets: Implications for the Moon. *Journal of Geophysical Research: Planets*, *119*(11), 2317–2330. https://doi.org/10.1002/2014JE004717
Ogawa, M. (2018a). The effects of magmatic redistribution of heat producing elements on the lunar mantle evolution inferred from numerical models that start from various initial states. *Planetary and Space Science*, *151*, 43–55. https://doi.org/10.1016/j.pss.2017.10.015
Ogawa, M. (2018b). Magmatic differentiation and convective stirring of the mantle in early planets: The effects of the magmatism-mantle upwelling feedback. *Geophysical Journal International*, *215*(3), 2144–2155. https://doi.org/10.1093/gji/ggy413
Ogawa, M. (2020). Magmatic differentiation and convective stirring of the mantle in early planets—2: Effects of the properties of mantle materials. *Geophysical Journal International*, *220*(2), 1409–1420. https://doi.org/10.1093/gji/ggz499
Pritchard, M. E., & Stevenson, D. J. (2000). Thermal aspects of a lunar origin by giant impact. In R. M. Canup, & K. Righter (Eds.), *Origin of the Earth and Moon* (pp. 179–196). University of Arizona Press. https://doi.org/10.2307/j.ctv1v7zdrp
Rapp, J. F., & Draper, D. S. (2018). Fractional crystallization of the lunar magma ocean: Updating the dominant paradigm. *Meteoritics & Planetary Science*, *53*(7), 1432–1455. https://doi.org/10.1111/maps.13086
Ringwood, A. E., & Kesson, S. E. (1976). A dynamic model for mare basalt petrogenesis. In *Proceedings of the lunar science conference* (Vol. 7, pp. 1697–1722).
Rufu, R., Aharonson, O., & Perets, H. B. (2017). A multiple-impact origin for the Moon. *Nature Geoscience*, *10*(2), 89–94. https://doi.org/10.1038/NGEO2866

Sakamaki, T., Ohtani, E., Urakawa, S., Suzuki, S., Katayama, Y., & Zhao, D. (2010). Density of high-Ti basalt magma at high pressure and origin of heterogeneities in the lunar mantle. *Earth and Planetary Science Letters*, *299*(3–4), 285–289. https://doi.org/10.1016/j.epsl.2010.09.007

Sawada, N., Morota, T., Kato, S., Ishihara, Y., & Hiramatsu, Y. (2016). Constraints on timing and magnitude of early global expansion of the Moon from topographic features in linear gravity anomaly areas. *Geophysical Research Letters*, *43*(10), 4865–4870. https://doi.org/10.1002/2016GL068966

Schwinger, S., & Breuer, D. (2022). Employing magma ocean crystallization models to constrain structure and composition of the lunar interior. *Physics of the Earth and Planetary Interiors*, *322*, 106831. https://doi.org/10.1016/j.pepi.2021.106831

Scott, T., & Kohlstedt, D. L. (2006). The effect of large melt fraction on the deformation behavior of peridotite. *Geophysical Monograph Series*, *246*(3–4), 177–187. https://doi.org/10.1016/j.epsl.2006.04.027

Shearer, C. K., Hess, P. C., Wieczorek, M. A., Pritchard, M. E., Parmentier, E. M., Borg, L. E., & Wiechert, U. (2006). Thermal and magmatic evolution of the Moon. *Reviews in Mineralogy and Geochemistry*, *60*(1), 365–518. https://doi.org/10.2138/rmg.2006.60.4

Shearer, C. K., & Papike, J. (1999). Magmatic evolution of the Moon. *American Mineralogist*, *84*(1), 1469–1494. https://doi.org/10.2138/am-1999-1001

Siegler, M. A., & Smrekar, S. E. (2014). Lunar heat flow: Regional prospective of the apollo landing sites. *Journal of Geophysical Research: Planets*, *119*(1), 47–63. https://doi.org/10.1002/2013JE004453

Siegler, M. A., Warren, P., Franco, K. L., Paige, D., Feng, J., & White, M. (2022). Lunar heat flow: Global predictions and reduced heat flux. *Journal of Geophysical Research: Planets*, *127*(9), e2022JE007182. https://doi.org/10.1029/2022JE007182

Snyder, G. A., Taylor, L. A., & Neal, C. R. (1992). A chemical model for generating the sources of mare basalts: Combined equilibrium and fractional crystallization of the lunar magmasphere. *Geochimica et Cosmochimica Acta*, *56*(10), 3809–3823. https://doi.org/10.1016/0016-7037(92)90172-F

Solomon, S. C. (1975). Mare volcanism and lunar crustal structure. In *Proceedings of the lunar science conference* (Vol. 6, pp. 1021–1042).

Solomon, S. C. (1986). *On the early thermal state of the Moon* (pp. 435–452). Lunar and Planetary Institute.

Solomon, S. C., & Chaiken, J. (1976). Thermal expansion and thermal stress in the Moon and terrestrial planets: Clues to early thermal history. In *Proceedings of the lunar science conference* (Vol. 7, pp. 3229–3243).

Solomon, S. C., & Head, J. W. (1979). Vertical movement in mare basins: Relation to mare emplacement, basin tectonics, and lunar thermal history. *Journal of Geophysical Research*, *84*(B4), 1667–1682. https://doi.org/10.1029/JB084iB04p01667

Solomon, S. C., & Toksöz, M. N. (1973). Internal constitution and evolution of the Moon. *Physics of the Earth and Planetary Interiors*, *7*(1), 15–38. https://doi.org/10.1016/0031-9201(73)90037-X

Sonett, C. P. (1982). Electromagnetic induction in the Moon. *Reviews of Geophysics*, *20*(3), 411. https://doi.org/10.1029/RG020i003p00411

Spohn, T., Konrad, W., Breuer, D., & Ziethe, R. (2001). The longevity of lunar volcanism: Implications of thermal evolution calculations with 2D and 3D mantle convection models. *Icarus*, *149*(1), 54–65. https://doi.org/10.1006/icar.2000.6514

Stegman, D. R., Jellinek, A. M., Zatman, S. A., Baumgardner, J. R., & Richards, M. A. (2003). An early lunar core dynamo driven by thermochemical mantle convection. *Nature*, *421*(6919), 143–146. https://doi.org/10.1038/nature01267

Stevenson, D. J. (1987). Origin of the Moon-the collision hypothesis. *Annual Review of Earth and Planetary Sciences*, *15*(1), 271–315. https://doi.org/10.1146/annurev.ea.15.050187.001415

Su, B., Yuan, J., Chen, Y., Yang, W., Mitchell, R. N., Hui, H., et al. (2022). Fusible mantle cumulates trigger young mare volcanism on the cooling Moon. *Science Advances*, *8*(42). https://doi.org/10.1126/sciadv.abn2103

Taguchi, M., Morota, T., & Kato, S. (2017). Lateral heterogeneity of lunar volcanic activity according to volumes of mare basalts in the farside basins. *Journal of Geophysical Research: Planets*, *122*(7), 1505–1521. https://doi.org/10.1002/2016JE005246

Tan, Y., & Harada, Y. (2021). Tidal constraints on the low-viscosity zone of the Moon. *Icarus*, *365*, 114361. https://doi.org/10.1016/j.icarus.2021.114361

Toksőz, M. N., & Solomon, S. C. (1973). Thermal history and evolution of the Moon. *The Moon*, *7*(3–4), 251–278. https://doi.org/10.1007/bf00564634

U, K., Hasumi, H., & Ogawa, M. (2022). Effects of magma-generation and migration on the expansion and contraction history of the Moon. *Earth Planets and Space*, *74*(78), 78. https://doi.org/10.1186/s40623-022-01631-4

U, K., Kameyama, M., & Ogawa, M. (2023). Numerical models of magmatism in the convective mantle of the Moon [Dataset]. Figshare. https://doi.org/10.6084/m9.figshare.22297921.v1

van der Bogert, C. H., Clark, J. D., Hiesinger, H., Banks, M. E., Watters, T. R., & Robinson, M. S. (2018). How old are lunar lobate scarps? 1. Seismic resetting of crater size-frequency distributions. *Icarus*, *306*, 225–242. https://doi.org/10.1016/j.icarus.2018.01.019

Vander Kaaden, K. E., Agee, C. B., & McCubbin, F. M. (2015). Density and compressibility of the molten lunar picritic glasses: Implications for the roles of ti and Fe in the structures of silicate melts. *Geochimica et Cosmochimica Acta*, *149*, 1–20. https://doi.org/10.1016/j.gca.2014.10.029

van Kan Parker, M., Sanloup, C., Sator, N., Guillot, B., Tronche, E. J., Perrillat, P., et al. (2012). Neutral buoyancy of titanium-rich melts in the deep lunar interior. *Nature Geoscience*, *5*(3), 186–189. https://doi.org/10.1038/ngeo1402

Viswanathan, V., Rambaux, N., Fienga, A., Laskar, J., & Gastineau, M. (2019). Observational constraint on the radius and oblateness of the lunar core-mantle boundary. *Geophysical Research Letters*, *46*(13), 7295–7303. https://doi.org/10.1029/2019GL082677

Watters, T. R., Robinson, M. S., Beyer, R. A., Banks, M. E., Bell, J. F., Pritchard, M. E., et al. (2010). Evidence of recent thrust faulting on the Moon revealed by the lunar reconnaissance orbiter camera. *Science*, *329*(5994), 936–940. https://doi.org/10.1126/science.1189590

Watters, T. R., Robinson, M. S., Collins, G. C., Banks, M. E., Daud, K., Williams, N. R., & Selvans, M. M. (2015). Global thrust faulting on the Moon and the influence of tidal stresses. *Geology*, *43*(10), 851–854. https://doi.org/10.1130/G37120.1

Weber, R. C., Lin, P.-Y., Garnero, E. J., Williams, Q., & Lognonné, P. (2011). Seismic detection of the lunar core. *Science*, *331*(6015), 309–312. https://doi.org/10.1126/science.1199375

Whitehead, J. A. J., & Luther, D. S. (1975). The generation and compaction of partially molten rock. *Journal of Geophysical Research*, *80*(5), 705–717. https://doi.org/10.1029/JB080i005p00705

Whitten, J. L., & Head, J. W. (2015). Lunar cryptomaria: Physical characteristics, distribution, and implications for ancient volcanism. *Icarus*, *247*, 150–171. https://doi.org/10.1016/j.icarus.2014.09.031

Wieczorek, M. A., Neumann, G. A., Nimmo, F., Kiefer, W. S., Taylor, G. J., Melosh, R. J., et al. (2013). The crust of the Moon as seen by GRAIL. *Science*, *339*(6029), 671–675. https://doi.org/10.1126/science.1199375

Wieczorek, M. A., & Phillips, R. J. (2000). The "procellarum KREEP terrane": Implications for mare volcanism and lunar evolution. *Journal of Geophysical Research*, *105*(E8), 20417–20430. https://doi.org/10.1029/1999JE001092

Wilson, L., & Head, J. W. (2003). Deep generation of magmatic gas on the Moon and implications for pyroclastic eruptions. *Icarus*, *30*(12). https://doi.org/10.1029/2002GL016082

Wilson, L., & Head, J. W. (2017). Generation, ascent and eruption of magma on the Moon: New insights into source depths, magma supply, intrusions and effusive/explosive eruptions (part 1: Theory). *Icarus*, *283*, 146–175. https://doi.org/10.1016/j.icarus.2015.12.039

Wood, J. A. (1972). Thermal history and early magmatism in the Moon. *Icarus*, *16*(2), 229–240. https://doi.org/10.1016/0019-1035(72)90070-X

Xu, M., Jing, Z., Van Orman, J. A., Yu, T., & Wang, Y. (2022). Experimental evidence supporting an overturned iron-titanium-rich melt layer in the deep lunar interior. *Geophysical Research Letters*, *49*(13), e2022GL099066. https://doi.org/10.1029/2022GL099066

Yan, J., Xu, L., Li, F., Matsumoto, K., Rodriguez, J. A. P., Miyamoto, H., & Dohm, J. M. (2015). Lunar core structure investigation: Implication of GRAIL gravity field model. *Advances in Space Research*, *55*(6), 1721–1727. https://doi.org/10.1016/j.asr.2014.12.038

Yanagisawa, T., Kameyama, M., & Ogawa, M. (2016). Numerical studies on convective stability and flow pattern in three-dimensional spherical mantle of terrestrial planets. *Geophysical Journal International*, *206*(3), 1526–1538. https://doi.org/10.1093/gji/ggw226

Yu, S., Tosi, N., Schwinger, S., Maurice, M., Breuer, D., & Xiao, L. (2019). Overturn of ilmenite-bearing cumulates in a rheologically weak lunar mantle. *Journal of Geophysical Research: Planets*, *124*(2), 418–436. https://doi.org/10.1029/2018je005739

Yue, Z., Michael, G. G., Di, K., & Liu, J. (2017). Global survey of lunar wrinkle ridge formation times. *Earth and Planetary Science Letters*, *477*, 14–20. https://doi.org/10.1016/j.epsl.2017.07.048

Zhang, N., Ding, M., Zhu, M.-H., Li, H., Li, H., & Yue, Z. (2022a). Lunar compositional asymmetry explained by mantle overturn following the South Pole–Aitken impact. *Nature Geoscience*, *15*(1), 37–41. https://doi.org/10.1038/s41561-021-00872-4

Zhang, N., Dygert, N., Liang, Y., & Parmentier, E. (2017). The effect of ilmenite viscosity on the dynamics and evolution of an overturned lunar cumulate mantle. *Geophysical Research Letters*, *44*(13), 6543–6552. https://doi.org/10.1002/2017GL073702

Zhang, N., Parmentier, E., & Liang, Y. (2013a). A 3-D numerical study of the thermal evolution of the Moon after cumulate mantle overturn: The importance of rheology and core solidification. *Journal of Geophysical Research: Planets*, *118*(9), 1789–1804. https://doi.org/10.1002/jgre.20121

Zhang, N., Parmentier, E., & Liang, Y. (2013b). Effects of lunar cumulate mantle overturn and megaregolith on the expansion and contraction history of the Moon. *Geophysical Research Letters*, *40*(19), 5019–5023. https://doi.org/10.1002/grl.50988

Zhang, W. B., Zhang, N., & Li, H. Y. (2022b). Abundances of lunar heat-producing elements constrained by a 3-D numerical model of titanium-rich basaltic eruption. *Chinese Journal of Geophysics*, *65*(1), 119–136. https://doi.org/10.6038/cjg2022P0753

Zhao, Y., de Vries, J., van den Berg, A. P., Jacobs, M. H. G., & van Westrenen, W. (2019). The participation of ilmenite-bearing cumulates in lunar mantle overturn. *Earth and Planetary Science Letters*, *511*(1), 1–11. https://doi.org/10.1016/j.epsl.2019.01.022

Zhong, S., Parmentier, E. M., & Zuber, M. T. (2000). A dynamic origin for the global asymmetry of lunar mare basalts. *Earth and Planetary Science Letters*, *177*(3–4), 131–140. https://doi.org/10.1016/S0012-821X(00)00041-8

Ziethe, R., Seiferlin, K., & Hiesinger, H. (2009). Duration and extent of lunar volcanism: Comparison of 3D convection models to mare basalt ages. *Planetary and Space Science*, *57*(7), 784–796. https://doi.org/10.1016/j.pss.2009.02.002